Multi-color fluorescence fluctuation spectroscopy in living cells via spectral detection

Valentin Dunsing*, Annett Petrich and Salvatore Chiantia*

University of Potsdam, Institute of Biochemistry and Biology, Karl-Liebknecht-Str. 24-25, 14476 Potsdam, Germany

*To whom correspondence should be addressed: dunsing@uni-potsdam.de, chiantia@uni-potsdam.de

Abstract:

Signaling pathways in biological systems rely on specific interactions between multiple biomolecules. Fluorescence fluctuation spectroscopy provides a powerful toolbox to quantify such interactions directly in living cells. Cross-correlation analysis of spectrally separated fluctuations provides information about inter-molecular interactions but is usually limited to two fluorophore species. Here, we present scanning fluorescence spectral correlation spectroscopy (SFSCS), a versatile approach that can be implemented on commercial confocal microscopes, allowing the investigation of interactions between multiple protein species at the plasma membrane. We demonstrate that SFSCS enables cross-talk-free cross-correlation, diffusion and oligomerization analysis of up to four protein species labeled with strongly overlapping fluorophores. As an example, we investigate the interactions of influenza A virus (IAV) matrix protein 2 with two cellular host factors simultaneously. We furthermore apply raster spectral image correlation spectroscopy for the simultaneous analysis of up to four species and determine the stoichiometry of ternary IAV polymerase complexes in the cell nucleus.

Abbreviations

ACF, autocorrelation function; CCF, cross-correlation function; CF, correlation function; D, diffusion coefficient; F(C)CS, fluorescence (cross-) correlation spectroscopy; FFS,

fluorescence fluctuation spectroscopy; (sc-)FL(C)CS, (single-color) fluorescence lifetime (cross) correlation spectroscopy; FP, fluorescent protein; FRET, fluorescence resonance energy transfer; FSCS, fluorescence spectral correlation spectroscopy; IAV, influenza A virus; M1, IAV matrix protein 1, M2, IAV matrix protein 2; mEGFP, monomeric enhanced green fluorescent protein; mEYFP, monomeric enhanced yellow fluorescent protein; mp, myristoylated and palmitoylated; HA, IAV hemagglutinin protein; PA, polymerase acidic protein; PB1/PB2, polymerase basic protein 1/2; PC, polymerase complex; p_f, fluorescence probability; PM, plasma membrane; RI(C)CS, raster image (cross-) correlation spectroscopy; ROI, region of interest; RSICS, raster spectral image correlation spectroscopy; SD, standard deviation; SF(C)CS, scanning fluorescence (cross-) correlation spectroscopy; SNR, signal-to-noise ratio; TRICS, triple raster image correlation spectroscopy

49 **INTRODUCTION**

50 Living cells rely on transport and interaction of biomolecules to perform their diverse functions.
51 To investigate the underlying molecular processes in the native cellular environment, minimally
52 invasive techniques are needed. Fluorescence fluctuation spectroscopy (FFS) approaches
53 provide a powerful toolbox that fulfills this aim (1–3). FFS takes advantage of inherent
54 molecular dynamics present in biological systems, for example diffusion, to obtain molecular
55 parameters from fluctuations of the signal emitted by an ensemble of fluorescent molecules.
56 More in detail, the temporal evolution of such fluctuations allows the quantification of
57 intracellular dynamics. In addition, concentration and oligomerization state of molecular
58 complexes can be determined by analyzing the magnitude of fluctuations. Finally, hetero-
59 interactions of different molecular species can be detected by cross-correlation analysis of
60 fluctuations emitted by spectrally separated fluorophores (4). Over the last two decades, several
61 experimental FFS schemes such as raster image (cross-) correlation spectroscopy (RI(C)CS)
62 (5, 6), (cross-correlation) Number&Brightness analysis (7, 8), and imaging FCS (9) have been
63 developed, extending the concept of traditional single-point fluorescence (cross-) correlation
64 spectroscopy (F(C)CS) (10). A further interesting example of FFS analysis relevant in the field
65 of cell biology is represented by scanning F(C)CS (SF(C)CS). Using a scanning path
66 perpendicular to the plasma membrane (PM), this technique provides enhanced stability and
67 the ability to probe slow membrane dynamics (11), protein interactions (12, 13) and
68 oligomerization (14) at the PM of cells.

69 FFS studies are conventionally limited to the analysis of two spectrally distinguished species,
70 due to i) broad emission spectra of fluorophores with consequent cross-talk artefacts, and ii)
71 limited overlap of detection/excitation geometries for labels with large spectral separation.
72 Generally, only few fluorescence-based methods are available to detect ternary or higher order
73 interactions of proteins (15–17). First *in vitro* approaches to perform FCS on more than two

74 species exploited different Stokes shifts of quantum dots (18) or fluorescent dyes excited with
75 a single laser line (19) or two-photon excitation (20, 21), coupled with detection on two or more
76 single photon counting detectors. Following an alternative conceptual approach, it was shown
77 *in vitro* that two spectrally strongly overlapping fluorophore species can be discriminated in
78 FCS by applying statistical filtering of detected photons based on spectrally resolved
79 (fluorescence spectral correlation spectroscopy, FSCS (22)) or fluorescence lifetime
80 (fluorescence lifetime correlation spectroscopy, FLCS (23–25)) detection. Such a framework
81 allows the minimization of cross-talk artefacts in FCCS measurements performed in living cells
82 (26). Recently, three-species implementations of RICCS and FCCS were successfully
83 demonstrated for the first time in living cells. Schrimpf et al. presented raster spectral image
84 correlation spectroscopy (RSICS), a powerful combination of RICS with spectral detection and
85 statistical filtering based on the emission spectra of mEGFP, mVenus and mCherry
86 fluorophores (27). Stefl et al. developed single-color fluorescence lifetime cross-correlation
87 spectroscopy (sc-FLCCS), taking advantage of several GFP variants characterized by short or
88 long fluorescence lifetimes (28). Using this elegant approach, three-species FCCS
89 measurements could be performed in yeast cells, with just two excitation lines.
90 Here, we explore the full potential of FSCS and RSICS. In particular, we present scanning
91 fluorescence spectral correlation spectroscopy (SFSCS), combining SFCS and FSCS. We show
92 that SFSCS enables cross-talk-free SFCCS measurements of two protein species at the PM of
93 living cells tagged with strongly overlapping fluorophores in the green or red region of the
94 visible spectrum, excited with a single excitation line. This approach results in correct estimates
95 of protein diffusion dynamics, oligomerization, and interactions between both species. Further,
96 we extend our approach to the analysis of three or four interacting partners: by performing
97 cross-correlation measurements on different fluorescent protein (FP) hetero-oligomers, we
98 demonstrate that up to four FP species can be simultaneously analyzed. We then apply this
99 scheme to simultaneously investigate the interaction of influenza A virus (IAV) matrix protein

100 2 (M2) with two cellular host factors, the tetraspanin CD9 and the autophagosome protein LC3,
101 co-expressed in the same cell. Finally, we extend RSICS for the detection of four molecular
102 species and quantify, for the first time directly in living cells, the complete stoichiometry of
103 ternary IAV polymerase complexes assembling in the nucleus, using three-species fluorescence
104 correlation and brightness analysis.
105
106
107

108 # RESULTS

109 **Cross-talk-free scanning SFSCS analysis of membrane-associated proteins using FPs with**
110 **strongly overlapping emission spectra and a single excitation wavelength**

111 To test the suitability of SFSCS to quantify interactions between membrane proteins tagged
112 with strongly spectrally overlapping fluorophores, we investigated HEK 293T cells co-
113 expressing mp-mEGFP and mp-mEYFP. These monomeric FPs are anchored independently to
114 the inner leaflet of the PM and their emission maxima are only ca. 20 nm apart (Fig.S3). The
115 signal originating from the two fluorophores was decomposed using spectral filters (Fig.S4A)
116 based on the emission spectra detected on cells expressing mp-mEGFP and mp-mEYFP
117 separately (Fig.S3). We then calculated autocorrelation functions (ACFs) and the cross-
118 correlation function (CCF) for signal fluctuations assigned to each fluorophore species.
119 Representative CFs for a typical measurement are shown in Fig.1A, indicating absence of
120 interactions and negligible cross-talk between the two FPs. In contrast, we observed substantial
121 CCFs when analyzing measurements on cells expressing mp-mEYFP-mEGFP hetero-dimers
122 (Fig.S5A). Overall, we obtained a relative cross-correlation (rel.cc.) of 0.72±0.12 (mean±SD,
123 n=22 cells) in the latter sample, compared to a vanishing rel.cc. of 0.02±0.04 (mean±SD, n=34
124 cells) in the negative control (Fig.1B). Comparison of two types of linker peptides (short
125 flexible or long rigid) between mEGFP and mEYFP showed that the linker length slightly
126 affected rel.cc. values obtained on hetero-dimers (Fig.S5C). FPs linked by a short peptide
127 displayed lower rel.cc., probably due to fluorescence resonance energy transfer (FRET), as
128 previously reported (29). Therefore, unless otherwise noted, similar long rigid linkers were
129 inserted in all constructs used in this study that contain multiple FPs (see Table S2).

130 Overlapping fluorescence emission from different species detected in the same channels
131 provides unwanted background signal and thus reduces the signal-to-noise ratio (SNR) of the
132 CFs (27). To assess to which extent the SNR depends on the relative concentration of mEGFP

133 and mEYFP fluorophores, we compared it between measurements on cells with different
134 relative expression levels of the two membrane constructs (Fig.1C). While the SNR of mEGFP
135 ACFs was only moderately affected by the presence of mEYFP signal (i.e. SNR ranging from
136 ca. 2.5 to 1.0, with 90% to 10% of the signal originating from mEGFP), the ACFs measured
137 for mEYFP showed strong noise when mEGFP was present in much higher amount (i.e. SNR
138 ranging from 2.5 to 0.2, with 90% to 10% of the signal originating from mEYFP).
139 Next, we tested whether the same approach can be used for FPs with overlapping emission in
140 the red region of the visible spectrum, which generally suffer from reduced SNR in FFS
141 applications (14, 30). Therefore, we performed SFSCS measurements on HEK 293T cells co-
142 expressing mp-mCherry2 and mp-mApple. Also the emission spectra of these FPs are shifted
143 by less than 20 nm (Fig.S3, spectral filters are shown in Fig.S4B). Correlation analysis resulted
144 generally in noisier CFs (Fig.1D) compared to mEGFP and mEYFP. Nevertheless, a
145 consistently negligible rel.cc. of 0.04±0.06 (mean±SD, n=24 cells) was observed. In contrast, a
146 high rel.cc. of 0.78±0.19 (mean±SD, n=18 cells) was obtained on cells expressing mp-
147 mCherry2-mApple hetero-dimers (Fig.1E, Fig.S5B). SNR analysis confirmed lower SNRs of
148 the CFs obtained for red FPs (Fig.1F) compared to mEGFP and mEYFP, with mApple
149 depending more weakly on the relative fluorescence signal than mCherry2 (i.e. ca. 2-fold
150 change for mApple vs. ca. 4-fold change for mCherry2, when the relative abundance changed
151 from 90% to 10%).
152

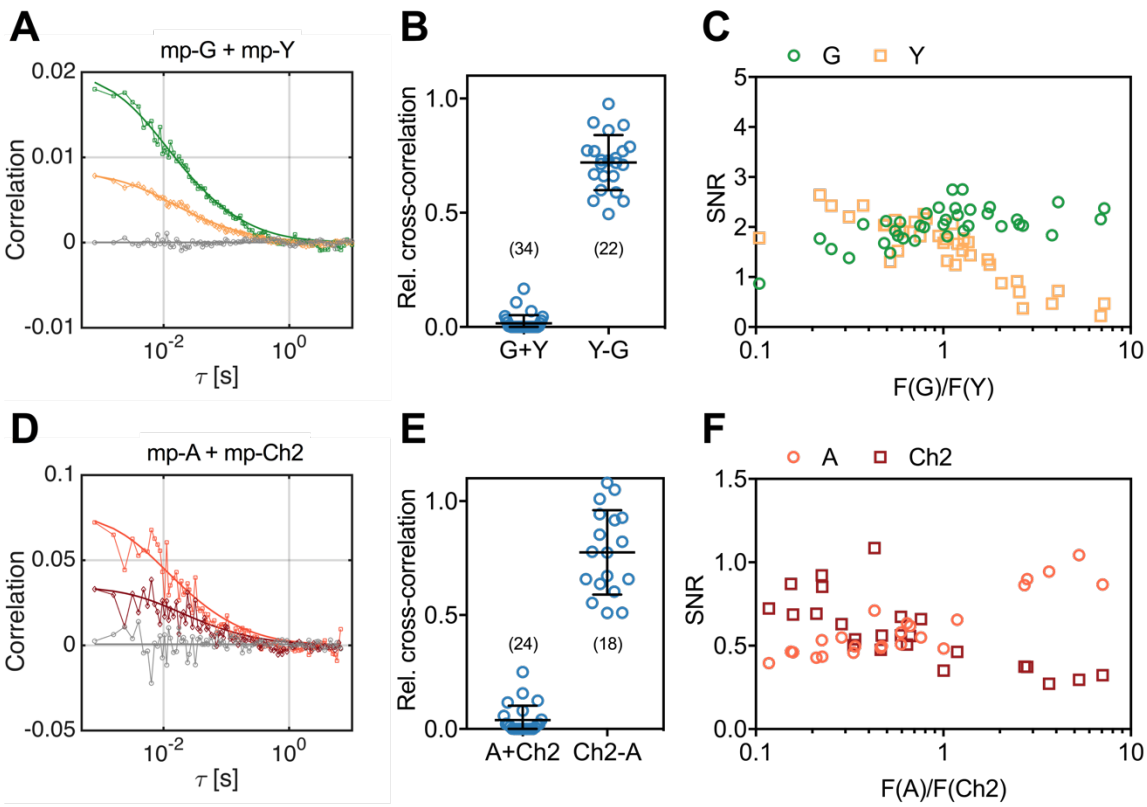

Figure 1. Cross-correlation and SNR analysis for two-species SFSCS measurements at the PM of HEK 293T cells, performed with FPs showing strongly overlapping emission spectra. (A) Representative CFs (green: ACF for mEGFP ("G"), yellow: ACF for mEYFP ("Y"), grey: CCF calculated for both fluorophore species) obtained from SFSCS measurements on the PM of HEK 293T cells co-expressing mp-mEGFP and mp-mEYFP. Solid thick lines show fits of a two-dimensional diffusion model to the CFs. **(B)** Relative cross-correlation values obtained from SFSCS measurements described in (A) ("G+Y") or on HEK 293T cells expressing mp-mEYFP-mEGFP hetero-dimers ("Y-G"). **(C)** SNR of ACFs for mEGFP (green) and mEYFP (yellow), obtained from SFSCS measurements described in (A), plotted as a function of the average ratio of detected mEGFP and mEYFP fluorescence. **(D)** Representative CFs (light red: ACF for mApple ("A"), dark red: ACF for mCherry2 ("Ch2"), grey: CCF calculated for both fluorophores) obtained from SFSCS measurements on the PM of HEK 293T cells co-expressing mp-mApple and mp-mCherry2. Solid thick lines show fits of a two-dimensional diffusion model to the CFs. **(E)** Relative cross-correlation values obtained from SFSCS measurements described in (D) ("A+Ch2") or on HEK 293T cells expressing mp-mCherry2-mApple hetero-dimers ("Ch2-A"). **(F)** SNR of ACFs for mApple (light red) and mCherry2 (dark red), obtained from SFSCS measurements described in (D), plotted as a function of the average ratio of detected mApple and mCherry2 fluorescence. Data are pooled from three (B) or two (E) independent experiments each. The number of cells measured is given in parentheses. Error bars represent mean±SD.

We furthermore verified that SFSCS analysis results in correct estimates of protein diffusion dynamics. To this aim, we co-expressed mEGFP-tagged IAV hemagglutinin spike transmembrane protein (HA-mEGFP) and mp-mEYFP. We then compared the diffusion times measured by SFSCS to the values obtained on cells expressing each of the two constructs separately (Fig.2A). For HA-mEGFP, an average diffusion time of 36±8 ms (mean±SD, n=18 cells) was determined in cells expressing both proteins. This value was comparable to that

178 measured for HA-mEGFP expressed separately (34±9 ms, mean±SD, n=21 cells). For mp-
179 mEYFP, diffusion times of 8±2 ms and 9±3 ms were measured in samples expressing both
180 proteins or just mp-mEYFP, respectively. In addition to diffusion analysis, we also analyzed
181 the cross-correlation of HA-mEGFP and mp-mEYFP signal for two-species measurements,
182 resulting in negligible rel.cc. values close to zero (Fig.S6). Hence, SFSCS yielded correct
183 estimates of diffusion dynamics and allowed to distinguish faster and slower diffusing protein
184 species tagged with spectrally strongly overlapping FPs.
185

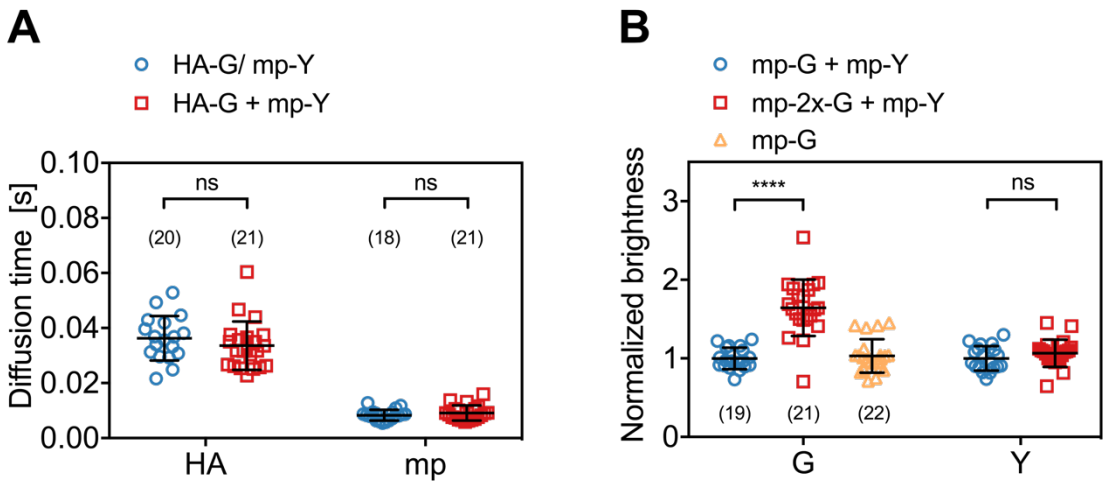

186
187 **Figure 2. Diffusion and molecular brightness analysis for two-species SFSCS measurements at the PM of**
188 **HEK 293T cells. (A)** Diffusion times obtained from SFSCS measurements on HEK 293T cells expressing either
189 IAV HA-mEGFP or mp-mEYFP separately (blue), or co-expressing both fusion proteins (red). **(B)** Normalized
190 molecular brightness values obtained from SFSCS measurements on HEK 293T cells co-expressing mp-mEGFP
191 and mp-mEYFP (blue), mp-2x-mEGFP and mp-mEYFP (red), or expressing mp-mEGFP alone (yellow).
192 Normalized brightness values were calculated by dividing molecular brightness values detected in each SFSCS
193 measurement by the average brightness obtained for mEGFP and mEYFP in cells co-expressing mp-mEGFP and
194 mp-mEYFP. Data are pooled from two independent experiments for each sample. The number of cells measured
195 is given in parentheses. Error bars represent mean±SD. Statistical significance was determined using Welch's
196 corrected two-tailed student's *t*-test (****P<0.0001, ns: not significant).
197

198 Finally, we evaluated the capability of SFSCS to precisely determine the molecular brightness,
199 as a measure of protein oligomerization. We compared the molecular brightness values for
200 mEGFP and mEYFP in samples co-expressing monomeric FP constructs mp-mEGFP and mp-
201 mEYFP with the values obtained for cells co-expressing mp-2x-mEGFP homo-dimers and mp-
202 mEYFP (Fig.2B). From SFSCS analysis of measurements in the latter sample, we obtained a
203 normalized molecular brightness of 1.64±0.36 (mean±SD, n=21 cells) for mEGFP, relative to

204 the brightness determined in the monomer sample (n=19 cells). This value is in agreement with
205 our previous quantification of the relative brightness of mEGFP homo-dimers, corresponding
206 to a fluorescence probability (p_f) of ca. 60-75% for mEGFP (14). The p_f is an empirical, FP-
207 specific parameter that was previously characterized for multiple FPs (14). It quantifies the
208 fraction of non-fluorescent FPs due to photophysical processes, such as transitions to long-lived
209 dark states, or slow FP maturation and needs to be taken into account to correctly determine the
210 oligomerization state of FP tagged protein complexes. As a reference for the absolute
211 brightness, we also determined the relative molecular brightness of mEGFP in cells expressing
212 mp-mEGFP alone, yielding a value of 1.03±0.21 (mean±SD, n=22 cells). Additionally, the
213 brightness values determined for mEYFP in both two-species samples were similar, with a
214 relative ratio of 1.07±0.18, as expected. This confirms that reliable brightness values were
215 obtained and that dimeric and monomeric species can be correctly identified.
216 In summary, these results demonstrate that SFSCS analysis of fluorescence fluctuations
217 successfully separates the contributions of FPs exhibiting strongly overlapping emission
218 spectra, yielding correct quantitative estimates of protein oligomerization and diffusion
219 dynamics.
220
221 **Simultaneous cross-correlation and brightness analysis for three spectrally overlapping**
222 **FPs at the PM**
223 In the previous section, we showed that SFSCS enables cross-talk-free cross-correlation
224 analysis of two fluorescent species excited with a single laser line, even in the case of strongly
225 overlapping emission spectra. To explore the full potential of SFSCS, we extended the approach
226 to systems containing three spectrally overlapping fluorophores. We excited mEGFP, mEYFP,
227 and mCherry2 with 488 nm and 561 nm lines simultaneously and detected their fluorescence
228 in 23 spectral bins in the range of 491 nm to 695 nm. We measured individual emission spectra
229 (Fig.S3) for single species samples to calculate three-species spectral filters (Fig.S4C), which

230 we then used to decompose the signal detected in cells expressing multiple FPs into the
231 contribution of each species.
232 As a first step, we performed three-species SFSCS measurements on HEK 293T cells co-
233 expressing mp-mEYFP with either i) mp-mEGFP and mp-mCherry2 (mp-G + mp-Y + mp-
234 Ch2) or ii) mp-mCherry2-mEGFP hetero-dimers (mp-Ch2-G + mp-Y). Additionally, we tested
235 a sample with cells expressing mp-mEYFP-mCherry2-mEGFP hetero-trimers (mp-Y-G-Ch2).
236 We then calculated ACFs for all three FP species and CCFs all fluorophore combinations,
237 respectively. In the first sample (mp-G + mp-Y + mp-Ch2), in which all three FPs are anchored
238 independently to the PM, we obtained CCFs fluctuating around zero for all fluorophore
239 combinations, as expected (Fig.3A). In the second sample (mp-Ch2-G + mp-Y), a substantial
240 cross-correlation was detected between mEGFP and mCherry2, whereas the other two
241 combinations resulted in CCFs fluctuating around zero (Fig.3B). In the hetero-trimer sample,
242 CCFs with low level of noise and amplitudes significantly above zero were successfully
243 obtained for all three fluorophore combinations (Fig.3C). From the amplitude ratios of the
244 ACFs and CCFs, we then calculated rel.cc. values for all measurements (Fig.3F). Negligible
245 rel.cc. values were obtained for all fluorophore combinations that were not expected to show
246 interactions, e.g. 0.05±0.08 (mean±SD, n=46 cells) between mEGFP and mEYFP signal in the
247 first sample. Low residual rel.cc. values obtained in a few measurements are likely an artefact
248 of the fitting procedure (caused by restriction of the correlation amplitude to positive values).
249 For noisy CCFs, this issue is responsible for low, but positive correlation amplitudes (and thus
250 rel.cc. values) even in the absence of significant correlation (i.e. for CCFs fluctuating around
251 zero), and a high uncertainty of this fit parameter. For mEGFP and mCherry2, similar rel.cc.
252 values of 0.45±0.06 (mean±SD, n=20 cells) and 0.56±0.08 (mean±SD, n=17 cells) were
253 observed in cells expressing mp-mCherry2-mEGFP hetero-dimers or mp-mEYFP-mCherry2-
254 mEGFP hetero-trimers. The minor difference could be attributed to different linker peptides
255 (i.e. long rigid linker between FPs in hetero-trimers and a short flexible linker in hetero-dimers),

256 increasing the degree of FRET between mEGFP and mCherry2 in hetero-dimers and reducing

257 the cross-correlation. The hetero-trimer sample showed high rel.cc. values also for the other

258 two fluorophore combinations: mEGFP and mEYFP (rel.cc.$_{G,Y}$=0.79±0.12) or mCherry2 and

259 mEYFP (rel.cc.$_{Y,Ch2}$=0.57±0.07).

260

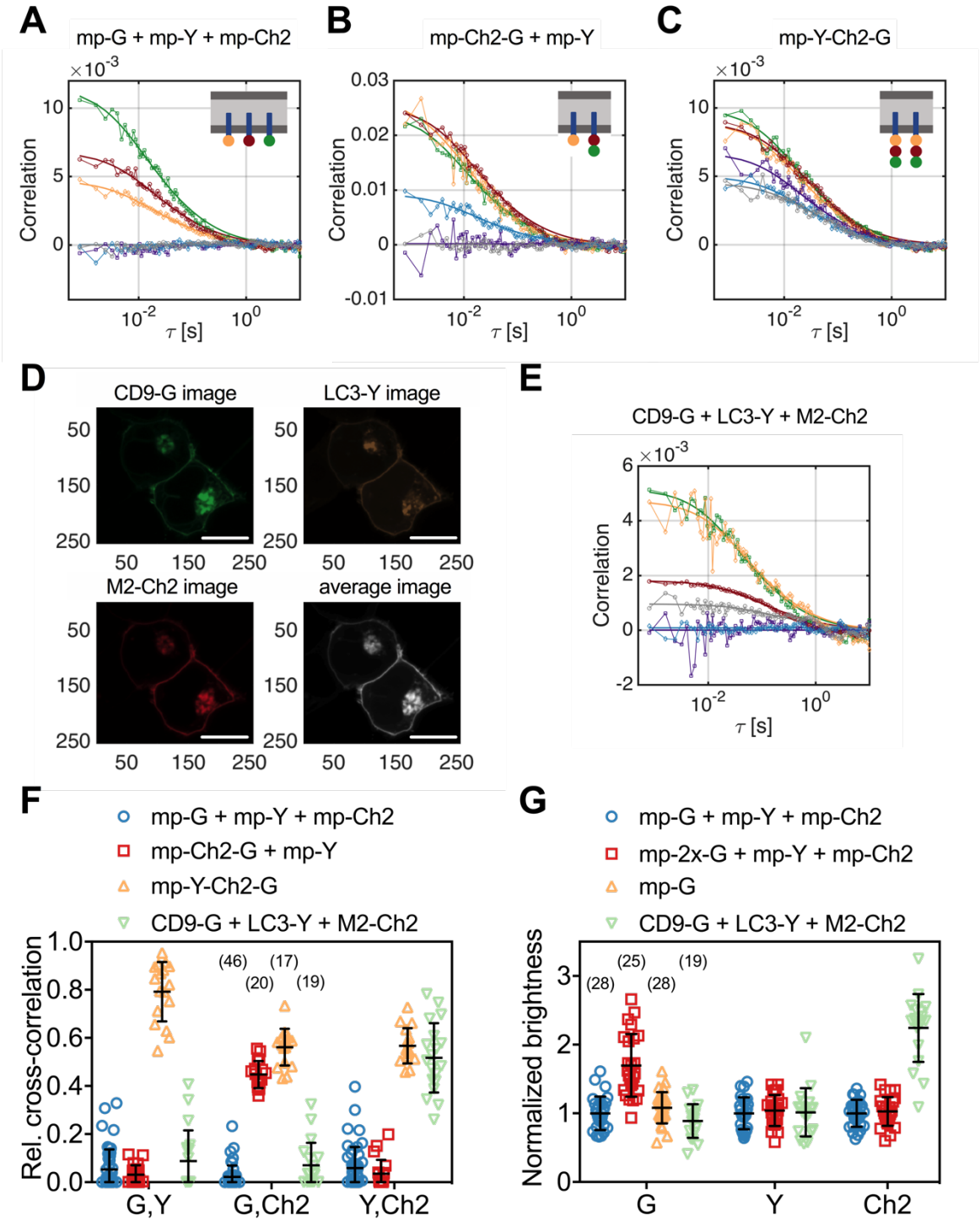

261

262 **Figure 3. Cross-correlation and molecular brightness analysis for three-species SFSCS measurements on**
263 **FP hetero-oligomers and IAV M2 at the PM of HEK 293T cells. (A-C)** Representative CFs (green/yellow/red:
264 ACFs for mEGFP ("G")/ mEYFP ("Y")/ mCherry2 ("Ch2"), purple/blue/grey: CCFs calculated for the pairs
265 mEGFP and mEYFP/ mEGFP and mCherry2/ mEYFP and mCherry2) obtained from three-species SFSCS
266 measurements on HEK 293T cells co-expressing mp-mEGFP, mp-mEYFP, and mCherry2 (A), mp-mCherry2-
267 mEGFP hetero-dimers and mp-mEYFP (B), or expressing mp-mEYFP-mCherry2-mEGFP hetero-trimers (C), as
268 illustrated in insets. Solid thick lines show fits of a two-dimensional diffusion model to the CFs. **(D)** Representative
269 fluorescence images of HEK 293T cells co-expressing CD9-mEGFP, LC3-mEYFP, and IAV protein M2-mCh2.
270 Spectral filtering and decomposition were performed to obtain a single image for each species. Scale bars are 5
271 µm. **(E)** Representative CFs (green/yellow/red: ACFs for mEGFP/mEYFP/mCherry2, purple/blue/grey: CCFs
272 calculated for the pairs mEGFP and mEYFP/ mEGFP and mCherry2/ mEYFP and mCherry2) obtained from three-
273 species SFSCS measurements on HEK 293T cells co-expressing CD9-mEGFP, LC3-mEYFP, and M2-mCh2.
274 Solid thick lines show fits of a two-dimensional diffusion model to the CFs. **(F)** Relative cross-correlation values
275 obtained from three-species SFSCS measurements described in (A-C) and I. **(G)** Normalized molecular brightness
276 values obtained from three-species SFSCS measurements on HEK 293T cells co-expressing mp-mEGFP, mp-
277 mEYFP, and mp-mCherry2 (blue), mp-2x-mEGFP, mp-mEYFP, and mp-mCherry2 (red), CD9-mEGFP, LC3-
278 mEYFP, and M2-mCh2 (green), or expressing mp-mEGFP alone (yellow). Normalized brightness values were
279 calculated by dividing the molecular brightness values detected in each SFSCS measurement by the average
280 brightness obtained for mEGFP, mEYFP, and mCherry2 in cells co-expressing mp-mEGFP, mp-mEYFP, and mp-
281 mCherry2. Data are pooled from two independent experiments for each sample. The number of cells measured is
282 given in parentheses. Error bars represent mean±SD.
283

284 In addition to cross-correlation analysis, we performed molecular brightness measurements on
285 samples containing three FP species. In particular, we compared molecular brightness values
286 obtained by SFSCS on HEK 293T cells co-expressing homo-dimeric mp-2x-mEGFP, mp-
287 mEYFP, and mp-mCherry2 (mp-2x-G + mp-Y + mp-Ch2) to the values measured on cells co-
288 expressing the three monomeric constructs mp-mEGFP, mp-mEYFP, and mp-mCherry2 (mp-
289 G + mp-Y + mp-Ch2). Whereas similar brightness values were obtained for mEYFP and
290 mCherry2 in both samples, e.g. relative brightness of 1.04±0.23 for mEYFP and 1.03±0.21 for
291 mCherry2 (mean±SD, n=25 cells/ n=28 cells), a higher brightness of 1.70±0.46 was measured
292 for mEGFP in the first sample (Fig.3G). This value corresponds to a p_f of ca. 70% for mEGFP,
293 as expected (14). To confirm that absolute brightness values are not influenced by the spectral
294 decomposition, we also determined the brightness of mEGFP in cells expressing mp-mEGFP
295 alone (Fig.3G), resulting in values close to 1 (1.08±0.23, mean±SD, n=28 cells).
296

297 **The IAV protein M2 interacts strongly with LC3 but not with CD9**

298 Having demonstrated the capability of SFSCS to successfully quantify protein interactions and
299 oligomerization, even in the case of three FPs with overlapping emission spectra, we applied

300 this approach in a biologically relevant context. In more detail, we investigated the interaction
301 of IAV channel protein M2 with the cellular host factors CD9 and LC3. CD9 belongs to the
302 family of tetraspanins and is supposedly involved in virus entry and virion assembly (31–33).
303 The autophagy marker protein LC3 was recently shown to be recruited to the PM in IAV-
304 infected cells (see also Fig.S7A,B), promoting filamentous budding and virion stability, thus
305 indicating a role of LC3 in virus assembly (34). To detect hetero-interactions between CD9,
306 LC3 and M2, we co-expressed the fluorescent fusion proteins CD9-mEGFP, LC3-mEYFP and
307 M2-mCherry2 (i.e. M2 carrying an mCherry2 tag at the extracellular terminus) in HEK 293T
308 cells (Fig.3D) and performed three-species SFSCS measurements at the PM (Fig.3E).
309 We then calculated rel.cc. values to quantify pair-wise interactions of the three proteins
310 (Fig.3F). The obtained rel.cc. values for CD9-mEGFP with LC3-mEYFP or M2-mCherry2
311 ($rel.cc._{CD9\text{-}G,LC3\text{-}Y}$=0.09±0.13,$rel.cc._{CD9\text{-}G,M2\text{-}Ch2}$=0.07±0.09, mean±SD, n=19 cells) were similar
312 to those of the negative cross-correlation control (i.e. cells co-expressing mp-mEGFP, mp-
313 mEYFP and mp-mCherry2, see previous paragraph). In contrast, we detected a substantial
314 rel.cc. of 0.52±0.14 for LC3-mEYFP and M2-mCherry2. This value was close (ca. 90% on
315 average) to that obtained for this fluorophore combination in measurements on FP hetero-
316 trimers, suggesting very strong association of LC3-mEYFP with M2-mCherry2. We
317 furthermore analyzed the molecular brightness for each species, normalized to the monomeric
318 references (Fig.3G). While CD9-mEGFP and LC3-mEYFP showed normalized brightness
319 values close to 1 ($B_{CD9\text{-}G}$=0.89±0.25, $B_{LC3\text{-}Y}$=1.02±0.35), suggesting that both proteins are
320 monomers, we observed significantly higher relative brightness values for M2-mCherry2 ($B_{M2\text{-}}$
321 $_{Ch2}$=2.24±0.49). Assuming a p_f of ca. 60% for mCherry2 (14), the determined relative brightness
322 corresponds to an oligomerization state of $\varepsilon_{M2-Ch2} = 3.1 \pm 0.8$, i.e. formation of M2 dimers to
323 tetramers at the PM.
324

325 **SFSCS allows simultaneous analysis of protein-protein interactions for four spectrally**
326 **overlapping FP species**
327 Having demonstrated robust three-species cross-correlation analysis, we aimed to further
328 explore the limits of SFSCS. We investigated therefore whether SFSCS can discriminate of
329 differential interactions between four species using the spectral emission patterns of mEGFP,
330 mEYFP, mApple and mCherry2 for spectral decomposition (Fig.S3, Fig.S4D). As a proof of
331 concept, we performed four-species measurements on three different samples: i) cells co-
332 expressing all four FPs independently as membrane-anchored proteins (mp-G + mp-Y + mp-A
333 + mp-Ch2), ii) cells co-expressing mp-mCherry2-mEGFP hetero-dimers, mp-mEYFP, and mp-
334 mApple (mp-Ch2-G + mp-Y + mp-A), iii) cells expressing mp-mEYFP-mCherry2-mEGFP-
335 mApple hetero-tetramers (mp-Y-Ch2-G-A). We then calculated four ACFs, six CCFs, and
336 rel.cc. values from the amplitude ratios of the ACFs and CCFs. For all fluorophore species,
337 ACFs with amplitudes significantly above zero were obtained. ACFs calculated for mEGFP
338 and mEYFP were characterized by a higher SNR compared to those for the red FPs mApple
339 and, in particular, mCherry2 (Fig.4A-C). Nevertheless, reasonable diffusion time values could
340 be determined for all species, showing the largest variation for mCherry2 (Fig.S8).
341 Noise levels of the CCFs were moderate (Fig.4D-F), yet allowing robust fitting and estimation
342 of cross-correlation amplitudes. Based on the determined rel.cc. values (Fig.4G), the different
343 samples could successfully be discriminated. In the first sample (mp-G + mp-Y + mp-A + mp-
344 Ch2), neglibile to very low values were obtained, i.e. at maximum 0.11±0.11 (mean±SD, n=12
345 cells) for mApple and mCherry2. In the second sample (mp-Ch2-G + mp-Y + mp-A), similarly
346 low rel.cc. values were obtained for all fluorophore combinations, e.g. 0.10±0.10 (mean±SD,
347 n=13 cells) for mApple and mCherry2, with the exception of mEGFP and mCherry2, showing
348 an average value of 0.55±0.13. For the hetero-tetramer sample, high rel.cc. values were
349 measured for all fluorophore combinations, ranging from 0.42±0.07 (mean±SD, n=15 cells) for
350 mEGFP and mApple to 0.78±0.08 for mEGFP and mEYFP. Notably, a significant rel.cc. of

0.53±0.10 was also determined for mApple and mCherry2 signals, i.e. from the CCFs exhibiting the lowest SNR.

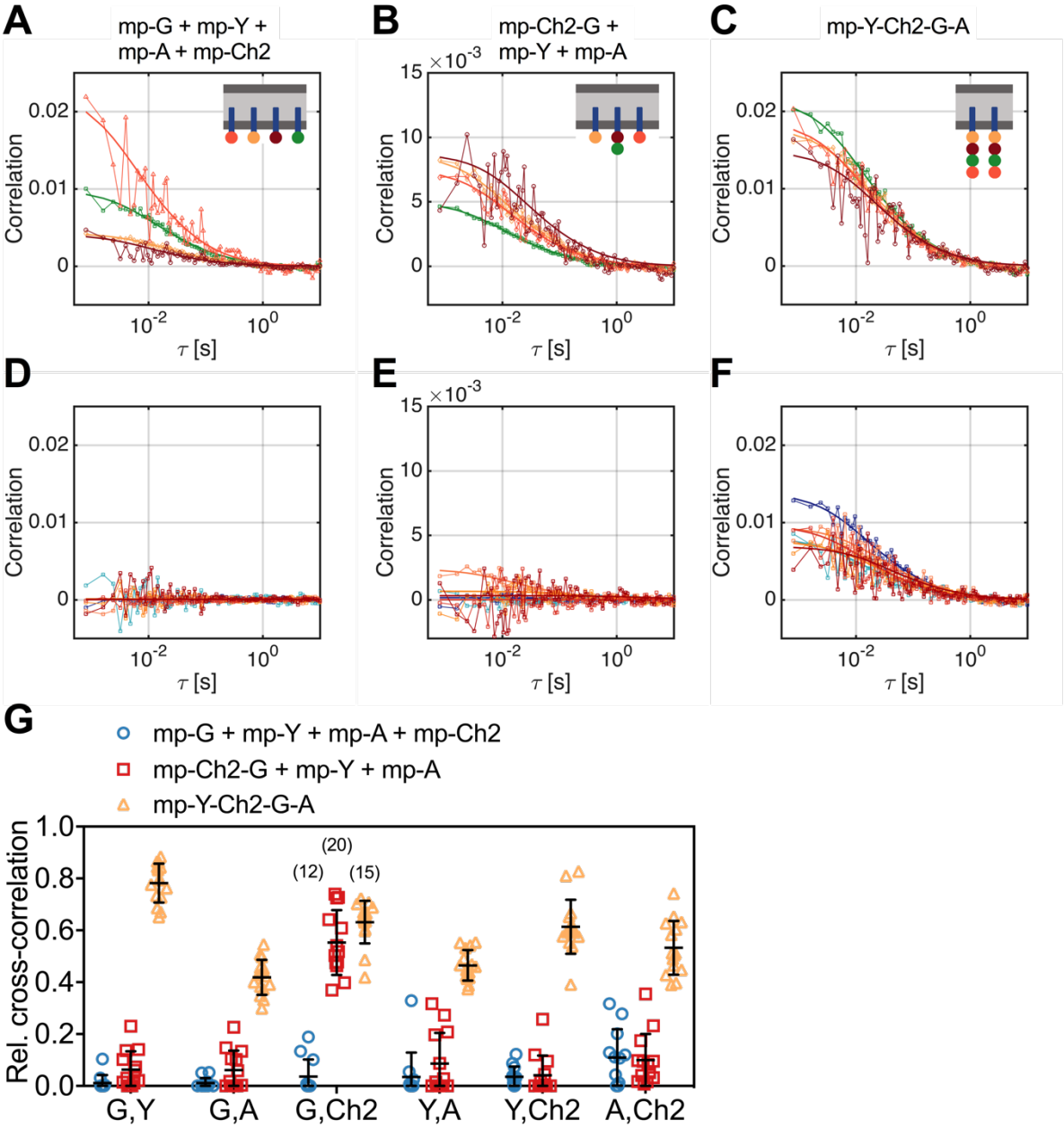

Figure 4. Cross-correlation analysis for four-species SFSCS measurements on FP hetero-oligomers in HEK 293T cells. (A-C) Representative ACFs (green/yellow/orange/red for mEGFP ("G")/ mEYFP ("Y")/ mApple ("A")/ mCherry2 ("Ch2")) obtained from four-species SFSCS measurements on HEK 293T cells co-expressing mp-mEGFP, mp-mEYFP, mp-mApple, and mCherry2 (A), mp-mCherry2-mEGFP hetero-dimers, mp-mEYFP, and mp-mApple (B), or expressing mp-mEYFP-mCherry2-mEGFP-mApple hetero-tetramers (C), as illustrated in insets. Solid thick lines show fits of a two-dimensional diffusion model to the CFs. **(D-F)** SFSCS CCFs (dark blue/ light blue/ orange/ yellow/ red/ dark red for CCFs calculated for mEGFP and mEYFP/ mEGFP and mApple/ mEGFP and mCherry2/ mEYFP and mApple/ mEYFP and mCherry2/ mApple and mCherry2) from measurements described in (A-C) (CCFs in (I(E)/(F) corresponding to ACFs shown in (A)/(B)/(C)). Solid thick lines show fits of a two-dimensional diffusion model to the CFs. **(G)** Relative cross-correlation values obtained from four-species SFSCS measurements described in (A-C). Data are pooled from two independent experiments. The number of cells measured is given in parentheses. Error bars represent mean±SD.

368 **RSICS can be extended to simultaneous detection of four fluorophore species**

369 Having identified a set of FPs that is compatible with four-species SFSCS, we aimed to extend
370 the recently presented RSICS method (27) to applications with four fluorophore species being
371 detected simultaneously. To test the effectiveness of this approach, we carried out
372 measurements in living A549 cells co-expressing mEGFP, mEYFP, mApple, and mCherry2 in
373 several configurations, similar to the SFSCS experiments presented in the previous paragraph.
374 In more detail, we performed four-species RSICS measurements on the following three
375 samples: i) cells co-expressing free mEGFP, mEYFP, mApple, and mCherry2 (1x-G + 1x-Y +
376 1x-A + 1x-Ch2), ii) cells co-expressing mCherry2-mEGFP and mEYFP-mApple hetero-dimers
377 (Ch2-G + Y-A), iii) cells expressing mEYFP-mCherry2-mEGFP-mApple hetero-tetramers (Y-
378 Ch2-G-A). Representative CFs obtained following RSICS analysis with arbitrary region
379 selection (35) are shown in Fig.5. In all samples, ACFs with amplitudes significantly above
380 zero were obtained, with the highest noise level detected for mCherry2 (Fig.5A,C,E). A three-
381 dimensional diffusion model could be successfully fitted to all detected ACFs.

382 Detected CCFs showed the expected pattern: all six CCFs were indistinguishable from noise
383 for the first sample with four independent FPs (Fig.5B), whereas large CCF amplitudes were
384 obtained for the pairs mEGFP and mCherry2, as well as mEYFP and mApple in the second
385 sample (Ch2-G + Y-A) (Fig.5D). Also, significantly large amplitudes were observed for all six
386 CCFs for the hetero-tetramer sample, albeit with different levels of noise. For example, the
387 lowest SNR was observed in CCFs for mApple and mCherry2 (Fig.5F).

388

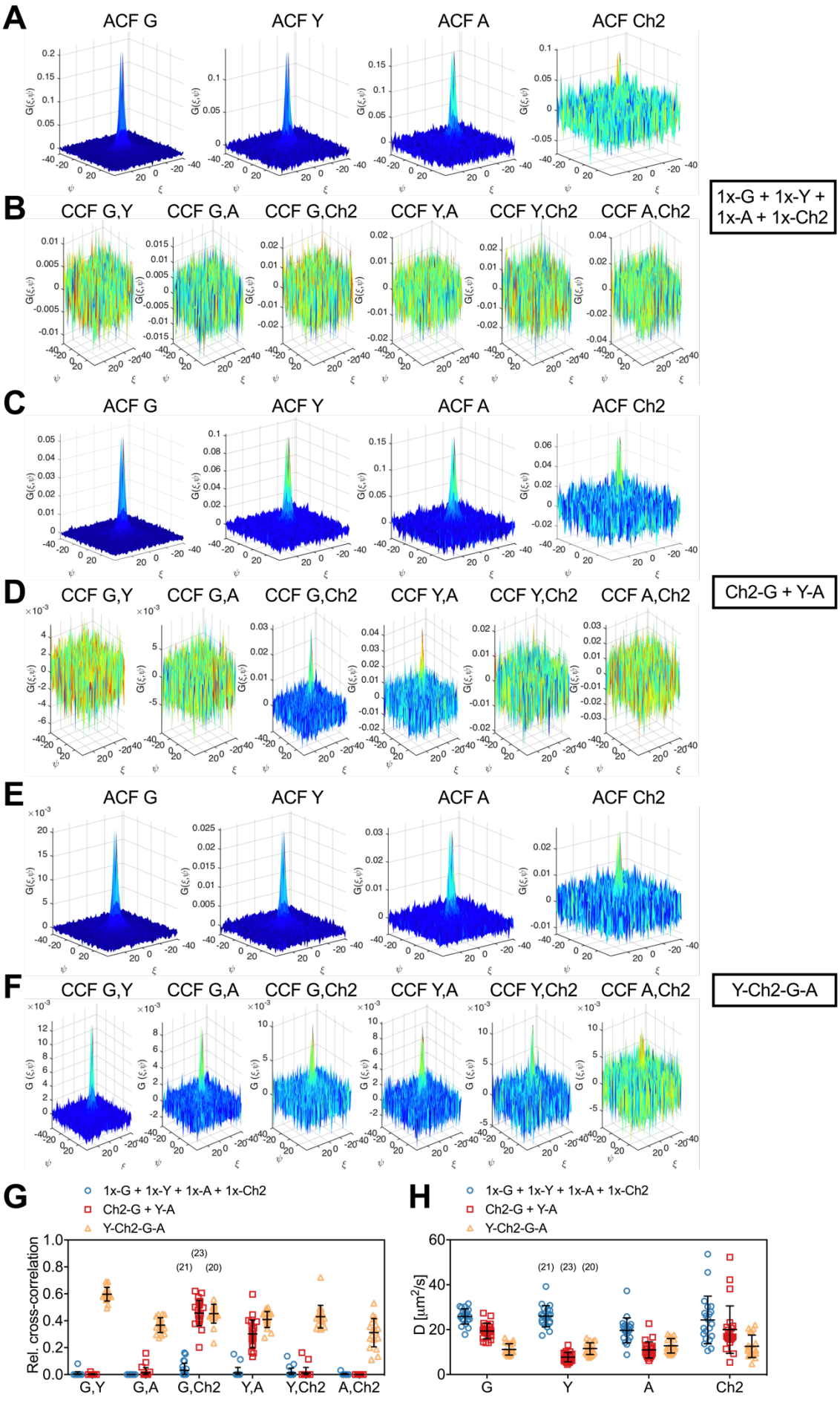
A
ACF G
ACF Y
ACF A
ACF Ch2
B
CCF G,Y
CCF G,A
CCF G,Ch2
CCF Y,A
CCF Y,Ch2
CCF A,Ch2
1x-G + 1x-Y + 1x-A + 1x-Ch2
C
ACF G
ACF Y
ACF A
ACF Ch2
D
CCF G,Y
CCF G,A
CCF G,Ch2
CCF Y,A
CCF Y,Ch2
CCF A,Ch2
Ch2-G + Y-A
E
ACF G
ACF Y
ACF A
ACF Ch2
F
CCF G,Y
CCF G,A
CCF G,Ch2
CCF Y,A
CCF Y,Ch2
CCF A,Ch2
Y-Ch2-G-A
G
1x-G + 1x-Y + 1x-A + 1x-Ch2
Ch2-G + Y-A
Y-Ch2-G-A
Rel. cross-correlation
(23)
(21) (20)
G,Y
G,A
G,Ch2
Y,A
Y,Ch2
A,Ch2
H
1x-G + 1x-Y + 1x-A + 1x-Ch2
Ch2-G + Y-A
Y-Ch2-G-A
D [μm²/s]
(21) (23) (20)
G
Y
A
Ch2

389

390 **Figure 5. Cross-correlation analysis for four-species RSICS measurements on FP hetero-oligomers**
391 **expressed in A549 cells. (A-F)** Representative RSICS spatial ACFs (A,C,E) and CCFs (B,D,F) obtained from
392 four-species RSICS measurements on A549 cells. Cells were co-expressing mEGFP ("G"), mEYFP ("Y"),
393 mApple ("A"), mCherry2 ("Ch2") (A,B), mCherry2-mEGFP and mEYFP-mApple heterodimers (C,D), or
394 mEYFP-mCherry2-mEGFP-mApple hetero-tetramers (E,F). **(G,H)** Relative cross-correlation values (G) and
395 diffusion coefficients (H) obtained from four-species RSICS measurements described in (A-F). Data are pooled
396 from two independent experiments. The number of cells measured is given in parentheses. Error bars represent
397 mean±SD.
398

399 From the amplitude ratios of ACFs and CCFs, we determined rel.cc. values (Fig.5G). This
400 analysis resulted in negligible values for the first sample (1x-G + 1x-Y + 1x-A + 1x-Ch2), e.g.
401 $rel.cc._{G,Ch2}$=0.03±0.05 (mean±SD, n=21 cells). For the second sample (Ch2-G + Y-A), values
402 significantly above zero, i.e. $rel.cc._{G,Ch2}$=0.46±0.09 (mean±SD, n=23 cells) and
403 $rel.cc._{Y,A}$=0.30±0.10, were only observed for two fluorophore pairs. For the third sample, cells
404 expressing mEYFP-mCherry2-mEGFP-mApple hetero-tetramers (Y-Ch2-G-A), rel.cc. values
405 significantly above zero were obtained for all FP pairs, ranging from $rel.cc._{A,Ch2}$=0.31±0.11
406 (mean±SD, n=20 cells) to $rel.cc._{G,Y}$=0.60±0.05. Notably, rel.cc. values obtained for the FP
407 species correlating in the second sample (Ch2-G + Y-A) were similar in the third sample (Y-
408 Ch2-G-A), e.g. $rel.cc._{G,Ch2}$=0.45±0.07 and $rel.cc._{Y,A}$=0.41±0.06. The lower rel.cc. value
409 measured for mEYFP and mApple in hetero-dimers (Ch2-G + Y-A) could be attributed to
410 different linker sequences (long rigid linker in hetero-dimers vs. mCherry2-mEGFP and three
411 long rigid linkers as spacer in hetero-tetramers (Y-Ch2-G-A)), possibly affecting FRET
412 between neighboring FPs.
413 Finally, we analyzed the diffusion dynamics of FP fusion proteins as determined from the
414 spatial dependence of the ACFs for the four fluorophore species. Diffusion coefficients (D)
415 obtained for mCherry2 showed the highest variation (Fig.5H), reflecting the reduced SNR for
416 this fluorophore. Nevertheless, similar average D values were determined for different
417 fluorophore species coupled as hetero-oligomers, e.g. D_G=19.4±3.4 $\mu m^2/s$ and D_{Ch2}=20±11
418 $\mu m^2/s$ (mean±SD, n=23 cells) for mEGFP-mCherry2 hetero-dimers, and D_G=11.2±2.5 $\mu m^2/s$,

419 D_Y=11.6±2.6 μm^2/s, D_A=12.8±3.2 μm^2/s, D_{Ch2}=12.6±5.0 μm^2/s (mean±SD, n=20 cells) for
420 hetero-tetramers.

421 **Cross-correlation and molecular brightness analysis via three-species RSICS provide**
422 **stoichiometry of IAV polymerase complex assembly**

423 To test the versatility of three-species RSICS, we quantified intracellular protein interactions
424 and stoichiometries in a biologically relevant context. As an example, we focused on the
425 assembly of the IAV polymerase complex (PC), consisting of the three subunits polymerase
426 acidic protein (PA), polymerase basic protein 1 (PB1), and 2 (PB2). A previous investigation
427 using FCCS suggested an assembly model in which PA and PB1 form hetero-dimers in the
428 cytoplasm of cells. These are imported into the nucleus and appear to interact with PB2 to form
429 hetero-trimeric complexes (36). Nevertheless, this analysis could only be performed between
430 two of the three subunits at the same time. Also, the stoichiometry of the complex was reported
431 only for one of the three subunits, i.e. PA protein dimerization. Here, we labeled all three
432 subunits using FP fusion constructs and co-expressed PA-mEYFP, PB1-mEGFP, and PB2-
433 mCherry2 in A549 cells. We then performed three-species RSICS measurements in the cell
434 nucleus, where all three proteins are enriched (Fig.6A). RSICS analysis was performed on an
435 arbitrarily-shaped homogeneous region of interest in the nucleus. We then calculated RSICS
436 ACFs (Fig.6B), CCFs (Fig.6C), and rel.cc. values (Fig.6D) for the three fluorophore
437 combinations. The determined rel.cc. values were compared to the values obtained on negative
438 controls (i.e. cells co-expressing free mEGFP, mEYFP, and mCherry) and positive controls (i.e.
439 cells expressing mEYFP-mCherry2-mEGFP hetero-trimers) (Fig.6D).

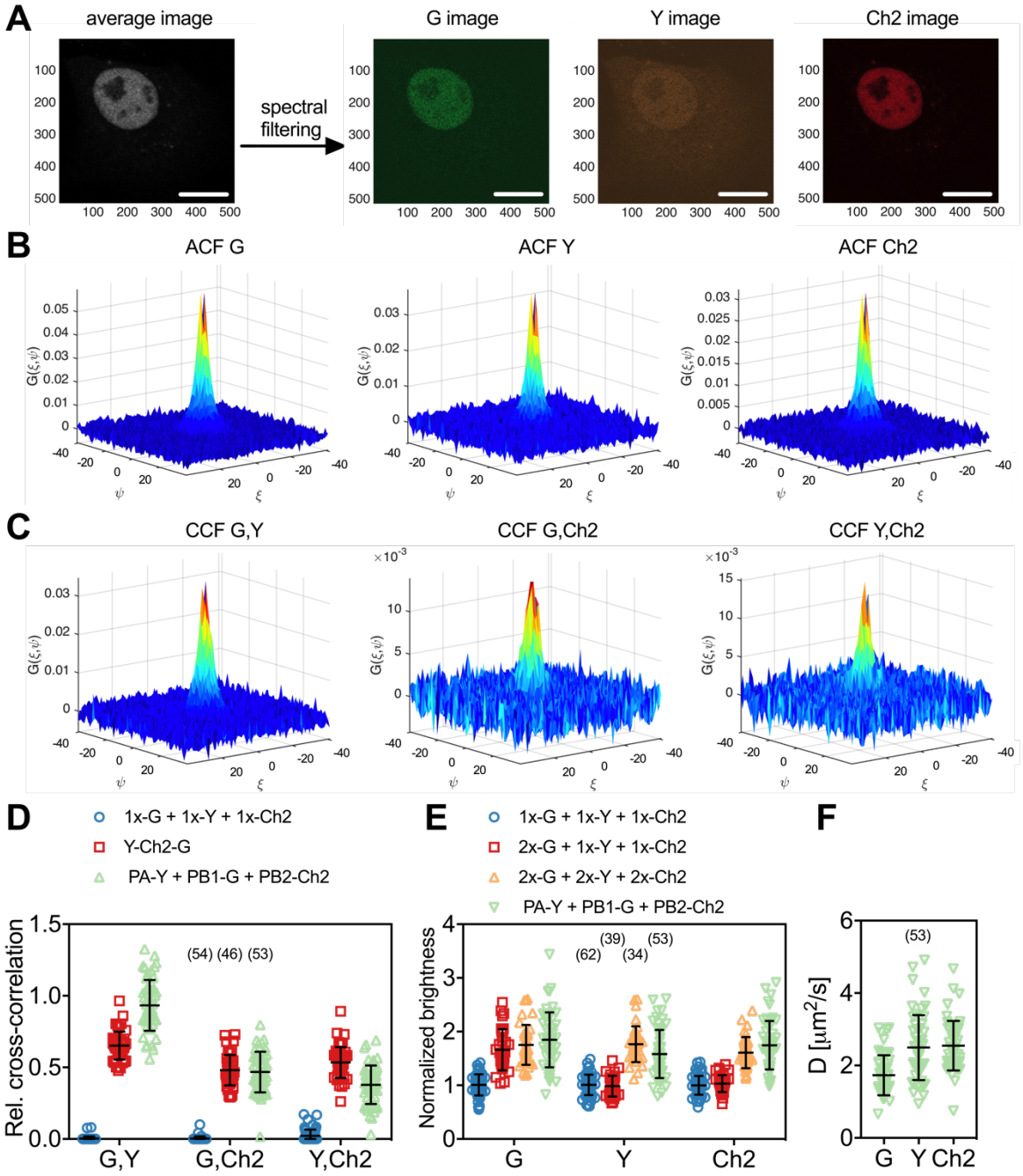

Figure 6. Three-species RSICS measurements on IAV polymerase complex and FP hetero-oligomers in the nucleus of A549 cells. (A) Representative fluorescence image (left) of A549 cells co-expressing FP-tagged IAV PC proteins PA-mEYFP, PB1-mEGFP, and PB2-mCherry2. Spectral filtering and decomposition result in a single image for each species (right), denoted with "Y", "G", and "Ch2". Scale bars are 10 µm. **(B,C)** Representative RSICS spatial ACFs (B) and CCFs (C) obtained from three-species RSICS measurements on A549 cells co-expressing PA-mEYFP, PB1-mEGFP, and PB2-mCherry2. **(D)** Relative cross-correlation values obtained from three-species RSICS measurements on A549 cells co-expressing mEGFP, mEYFP, and mCherry2 (blue), PA-mEYFP, PB1-mEGFP, PB2-mCherry2 (green), or expressing mEYFP-mCherry2-mEGFP hetero-trimers (red). Data are pooled from four independent experiments. **(E)** Normalized molecular brightness values obtained from three-species RSICS measurements on A549 cells co-expressing mEGFP, mEYFP, and mCherry2 (blue), 2x-mEGFP, mEYFP, and mCherry2 (red), 2x-mEGFP, 2x-mEYFP, 2x-mCherry2 (yellow), or PA-mEYFP, PB1-mEGFP, and PB2-mCherry2 (green). Data are pooled from three (2x-mEGFP + mEYFP + mCherry2, 2x-mEGFP + 2x-mEYFP + 2x-mCherry2), four (PA-mEYFP + PB1-mEGFP + PB2-mCherry2), or five (mEGFP + mEYFP + mCherry2) independent experiments. **(F)** Diffusion coefficients obtained from three-species RSICS measurements on A549 cells co-expressing PA-mEYFP, PB1-mEGFP, and PB2-mCherry2. Data are pooled from four independent experiments. For (D)-(F), the number of cells measured is given in parentheses. Error bars represent mean±SD.

458 For the polymerase sample, high rel.cc. values were observed for all combinations: rel.cc.$_{PB1-G,PA-Y}$=0.93±0.18 (mean±SD, n=53 cells), rel.cc.$_{PB1-G,PB2-Ch2}$=0.47±0.14, rel.cc.$_{PA-Y,PB2-Ch2}$=0.39±0.14. For the positive control, similar values were observed for mEGFP and mCherry2, rel.cc.$_{G,Ch2}$=0.48±0.11 (mean±SD, n=46 cells), whereas the values were higher than that measured for PCs for mEYFP and mCherry2, rel.cc.$_{Y,Ch2}$=0.53±0.11, and lower for mEGFP and mEYFP, rel.cc.$_{G,Y}$=0.65±0.10. The lower average rel.cc. between PA-mEYFP and PB2-mCherry2 compared to the positive control indicates the presence of a minor fraction of non-interacting PA and PB2. These proteins could be present in the nucleus in unbound form when expressed in higher amount than PB1, since both PA and PB2 localize in the nucleus individually and were previously shown not to interact when both present without PB1 (36). This explanation is supported by the correlation between rel.cc.$_{PA-Y,PB2-Ch2}$ and the relative abundance of PB1-mEGFP (Fig.S9A). Also, the observation that PB1 is only transported to the nucleus in complex with PA is confirmed by the lower concentration of PB1-mEGFP compared to PA-mEYFP in the nuclei of all measured cells (Fig.S9A). Thus, the fraction of PB1-mEGFP bound to PA-mEYFP should be as high as the positive control, for a 1:1 stoichiometry. The observation of higher rel.cc. between mEGFP and mEYFP for the polymerase subunits indicates higher order interactions, i.e. higher stoichiometry than 1:1 (37).

To quantify the stoichiometry of the PC directly, we analyzed the molecular brightness of RSICS measurements for all three fluorophore species. We normalized the obtained values to the average values determined by RSICS on cells co-expressing monomeric mEGFP, mEYFP, and mCherry2, measured on the same day. To test whether RSICS can be used to obtain reliable brightness/oligomerization values for all fluorophore species, we first performed control experiments on cells co-expressing either i) 2x-mEGFP homo-dimers with mEYFP and mCherry monomers (2x-G + 1x-Y + 1x-Ch2) or ii) the three homo-dimers 2x-mEGFP, 2x-mEYFP, and 2x-mCherry2 (2x-G + 2x-Y + 2x-Ch2). In the first sample, we observed an increased relative brightness of 1.67±0.38 (mean±SD, n=34 cells) for mEGFP, whereas values

484 around 1 were obtained for mEYFP and mCherry2. This confirmed the presence of mEGFP
485 dimers as well as mEYFP and mCherry2 monomers in this control sample, as expected
486 (Fig.6E). In the sample containing all three homo-dimers, increased relative brightness values
487 were observed for all fluorophore species: 1.75±0.37 (mean±SD, n=39 cells) for mEGFP,
488 1.77±0.33 for mEYFP, and 1.61±0.29 for mCherry2. These values indicate successful
489 determination of the dimeric state of all three FP homo-dimers and are in good agreement with
490 previous brightness measurements on homo-dimers of mEGFP, mEYFP and mCherry2,
491 corresponding to p_f values of 60-75% (14). Next, we proceeded with the analysis of PC
492 oligomerization. For each polymerase subunit, relative brightness values close to the values of
493 homo-dimers were observed. Assuming p_f values of 75%, 77%, and 61% (as calculated from
494 the determined relative brightness values of homo-dimers) for mEGFP, mEYFP, and
495 mCherry2, respectively, p_f corrected normalized brightness values of $\varepsilon_{PB1-G} = 2.1 \pm 0.7$
496 (mean±SD, n=53 cells), $\varepsilon_{PA-Y} = 1.8 \pm 0.6$, and $\varepsilon_{PB2-Ch2} = 2.2 \pm 0.7$ were obtained (see
497 methods for details). These results suggest a 2:2:2 stoichiometry of the IAV PC subunits.
498 Finally, we analyzed the diffusion dynamics of PCs via RSICS (Fig.6F). The average D
499 measured for PB1-mEGFP, D_{PB1-G}=1.7±0.6 $\mu m^2/s$ (mean±SD, n=53 cells), was ca. 30% lower
500 than the diffusion coefficients determined for PA-mEYFP- and PB2-mCherry2 (D_{PA-Y}=2.5±0.9
501 $\mu m^2/s$ and $D_{PB2-Ch2}$=2.6±0.7 $\mu m^2/s$). This observation is compatible with the above-mentioned
502 presence of a minor fraction of unbound (and thus faster diffusing) PA and PB2 (likely in cells
503 with a lower amount of PB1). A more detailed analysis of the data confirmed this interpretation:
504 The molecular brightness and diffusion coefficient of PA-mEYFP depended on the relative
505 concentration of PB1-mEGFP and PA-mEYFP, i.e. lower brightness and higher diffusion
506 coefficients were obtained in cells where PA-mEYFP was present at much higher
507 concentrations than PB1-mEGFP (Fig.S7B,C).
508

509 **Triple raster image correlation spectroscopy (TRICS) analysis provides direct evidence**
510 **for assembly of ternary IAV polymerase complexes**

511 To directly confirm that IAV PC subunits form ternary complexes in the cell nucleus, we
512 implemented a triple-correlation analysis (i.e. TRICS) to detect coincident fluctuations of the
513 signal emitted by mEGFP-, mEYFP- and mCherry2-tagged proteins. A similar analysis has
514 previously been presented for three-channel FCS measurements (e.g. fluorescence triple
515 correlation spectroscopy (21), triple-color coincidence analysis (20)), but was so far limited to
516 *in vitro* systems such as purified proteins (21) or DNA oligonucleotides (20) labeled with
517 organic dyes. We performed TRICS on data obtained on cells co-expressing PC subunits PA-
518 mEYFP, PB1-mEGFP, and PB2-mCherry2 or cells co-expressing free mEGFP, mEYFP, and
519 mCherry, as a negative triple-correlation control. To evaluate ternary complex formation, we
520 quantified the relative triple-correlation (rel.3C., see Materials and Methods) for both samples
521 from the amplitudes of the ACFs and triple-correlation functions (3CFs). Fig.7A and B show
522 representative 3CFs for the negative control and the PC sample, respectively. For the negative
523 control, we obtained rel.3C. values fluctuating around zero (Fig.7C), rel.3C.=-0.02±0.54
524 (mean±SD, n=49 cells). In contrast, significantly higher, positive rel.3C. values were obtained
525 for the polymerase samples, rel.3C.=0.43±0.38 (mean±SD, n=53 cells). The detection of
526 ternary complexes is limited by non-fluorescent FPs, i.e. only a fraction of ternary complexes
527 present in a sample will emit coincident signals for all three FP species. In addition, imperfect
528 overlap of the detection volumes for each channel will further reduce the fraction of ternary
529 complexes that can be detected by TRICS. We therefore performed an approximate calculation
530 of the expected rel.3C. value for a sample containing 100% ternary complexes assuming a p_f of
531 0.7 for each FP species and estimating the reduction due to imperfect overlap from the pair-
532 wise rel.cc. values detected on the positive cross-correlation control (see SI, paragraph 3 for
533 details). For a 2:2:2 stoichiometry, we obtained an estimated rel.3C. of 0.48, i.e. only slightly
534 higher than the average value determined experimentally for IAV PCs. Thus, we estimate that

around 90% of PC subunits undergo ternary complex formation in the cell nucleus when all subunits are present.

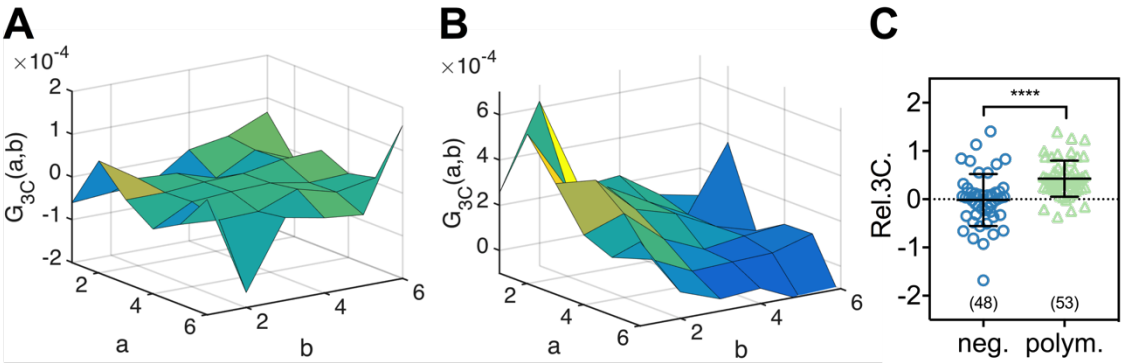

Figure 7. TRICS reveals the formation of ternary IAV polymerase hetero-complexes in the nucleus of A549 cells. (A,B) Representative 3CFs obtained from TRICS measurements on A549 cells co-expressing mEGFP, mEYFP, and mCherry2 ("neg.") (A) or co-expressing PA-mEYFP, PB1-mEGFP, and PB2-mCherry2 ("polym.") (B). The axes *a* and *b* indicate shifts in the x and y direction respectively, across the three detection channels, as described in the Materials and Methods. (C) Relative triple-correlation (rel.3C.) values obtained from the measurements described in (A,B). The number of cells measured is given in parentheses. Error bars represent mean±SD. Statistical significance was determined using Welch's corrected two-tailed student's *t*-test (****$P<0.0001$).

550 **DISCUSSION**

551 In this work, we combine FFS techniques with spectral detection to perform multi-color studies
552 of protein interactions and dynamics in living cells. In particular, we present SFSCS, a
553 combination of FSCS (22) and lateral scanning FCS (11). We show that SFSCS allows cross-
554 talk-free measurements of protein interactions and diffusion dynamics at the PM of cells and
555 demonstrate that it is capable of detecting three or four species simultaneously. Furthermore,
556 we extend RSICS (27) to investigate four fluorophore species and apply this approach to
557 determine the stoichiometry of higher order protein complexes assembling in the cell nucleus.
558 Notably, the technical approaches can be carried out on a standard confocal microscope,
559 equipped with a spectral photon counting detector system.

560 In the first part, we present two-species SFSCS using a single excitation wavelength and
561 strongly overlapping fluorophores. Compared to the conventional implementation of FCCS
562 with two excitation lasers and two detectors, SFSCS has substantial advantages, similar to the
563 recently presented sc-FLCCS (28). Since it requires a single excitation line and is compatible
564 with spectrally strongly overlapping FPs, it circumvents optical limitations such as imperfect
565 overlap of the observation volumes. This is evident from higher rel.cc. values of 70-80%
566 measured for mEGFP and mEYFP coupled in FP hetero-oligomers compared to 45-60%
567 observed for mEGFP and mCherry2. Rel.cc. values below 60% for green and red FPs were also
568 observed with single-wavelength excitation (29, 38), indicating that overlap of both excitation
569 and detection volumes (the latter requiring FPs with similar emission spectra) is required to
570 maximize the achievable cross-correlation (29). Notably, two-species SFSCS can not only
571 successfully discriminate between mEGFP and mEYFP, but is also applicable when using the
572 red FPs mApple and mCherry2. These two FPs were successfully used in several FFS studies
573 (14, 30, 39), providing the best compromise between brightness, maturation and photostability

574 among available red FPs, which generally suffer from reduced SNR compared to FPs emitting
575 in the green or yellow part of the optical spectrum (13, 14, 40).
576 In comparison to sc-FLCCS, it may be more robust to discriminate fluorophores based on
577 spectra rather than lifetimes, which can be strongly affected by FRET (28). The emission
578 spectra of the FPs utilized in this study did not depend on cell lines or subcellular localization
579 (Fig.S3) and showed no (mEGFP, mEYFP) or little (mApple, mCherry2) variation with pH
580 over a range of 5.0 to 9.2. (Fig.S10). For red FPs, specifically mApple, a red shift appeared at
581 more acidic pH, in agreement with previous studies (41). This aspect should be considered for
582 specific applications, e.g. RSICS in the cytoplasm containing acidic compartments such as
583 lysosomes. Generally, spectral approaches require accurate detection of photons in each
584 spectral bin. A previous study using the same detection system reported intrinsic cross-talk
585 between adjacent spectral bins (30). However, since the methodology presented here is based
586 on temporal (SFSCS) or spatial (RSICS) correlation (both excluding the correlation at zero time
587 or spatial lag), this issue can be neglected in our analysis.
588 A major limitation of SFSCS is the reduced SNR of the CFs (see Fig.1) caused by the statistical
589 filtering of the signal emitted by spectrally overlapping fluorophore species (see Fig.S4). This
590 limitation applies to all FFS methods that discriminate different fluorophore species based on
591 spectral (e.g. FSCS (22), RSICS (27)) or lifetime patterns (e.g. sc-FLCCS (28)). The increase
592 in noise depends on the spectral (or lifetime) overlap of different species and is more prominent
593 for species that completely lack "pure" channels, i.e. detection channels in which the majority
594 of photons can be univocally assigned to a single species (27). In sc-FLCCS, this issue
595 particularly compromises the SNR of short lifetime species (28), since photons of longer
596 lifetime species are detected in all "short lifetime" channels at substantial relative numbers. In
597 these conditions, sc-FLCCS could not provide reliable results with 6-fold (or higher) difference
598 in relative protein abundance, even though the lower abundant protein was tagged with the
599 brighter, longer lifetime FP (28). Similarly in SFSCS, CFs corresponding to mEYFP or

600 mCherry2 were most prone to noise (Fig.1C,F), since all channels that contain, e.g., mEYFP
601 signal also contain mEGFP signal (Fig.S3). In our experiments, cross-talk-free SFSCS analysis
602 with two species excited with a single excitation wavelength could be performed for relative
603 intensity levels as low as 1:10 (mEGFP/mEYFP) or 1:5 (mApple/mCherry2). In this range,
604 SFSCS not only enabled the quantification of protein interactions via cross-correlation analysis,
605 but also yielded correct estimates of protein diffusion dynamics and oligomerization at the PM.
606 An improvement of the allowed relative concentration range can be achieved by using brighter
607 or more photostable fluorophores, e.g. organic dyes, compensating for reduced SNR due to
608 statistical filtering. Alternatively, FP tags could be selected based on proteins oligomerization
609 state, e.g. monomeric proteins exhibiting low molecular brightness should be tagged with
610 fluorophores that are less prone to noise. It should be noted that the limitation of reduced SNR
611 due to excess signal from another species also applies to conventional dual-color FCCS: bleed-
612 through from green to red channels can be corrected on average, but reduces the SNR in red
613 channels (42), unless more sophisticated schemes such as pulsed interleaved excitation (43, 44)
614 are applied.
615 Having demonstrated that two-species SFSCS is feasible with a single excitation wavelength
616 in the green (mEGFP, mEYFP) or red (mApple, mCherry2) part of the visible spectrum, we
617 finally implemented three- and four-species SFSCS as well as four-species RSICS. Three- and
618 four-species SFSCS/ RSICS do not further compromise the SNR of CFs detected for mEGFP
619 and mEYFP, but may additionally reduce the SNR of CFs corresponding to red FPs (in
620 particular when mEGFP and/ or mEYFP concentration is much higher than that of red FPs).
621 For this reason, three- and four-species analysis was restricted to cells with relative average
622 intensity levels of 1:5 or less between species with adjacent emission spectra. In this range, the
623 increase in noise due to statistical filtering was moderate and benefited from the fairly large
624 spectral separation of green/yellow and red emission. In addition, the higher molecular
625 brightness of mApple (compared to mCherry2) compensated for the larger overlap of this FP

626 with the tail of mEYFP emission. The excitation power for red FPs was generally limited by
627 the lower photostability of mApple, which could be responsible for consistently lower rel.cc.
628 values of mEGFP or mEYFP with mApple than with mCherry2. Nevertheless, four-species
629 SFSCS and RSICS could successfully resolve different combinations of strongly overlapping
630 FP hetero-oligomers, e.g. a mixture of mEGFP-mCherry2 and mEYFP-mApple hetero-dimers,
631 at the PM or in the cytoplasm of cells. To explore the interaction of four different FP-tagged
632 proteins, four-species FFS may substantially reduce the experimental effort, because all pair-
633 wise interactions can be quantified in a single measurement (instead of six separate
634 conventional two-species FCCS measurements). Yet, weak interaction of proteins, i.e. a low
635 amount of hetero-complexes compared to a high amount of unbound proteins, may not be
636 detectable, due to the large noise of the CCF in this case. The SNR might be further
637 compromised by slow FP maturation or dark FP states, limiting the amount of complexes that
638 simultaneously emit fluorescence of all bound FP species (14). Ultimately, the mentioned
639 limitations currently restrict SFSCS and RSICS to four FP species. The approaches would thus
640 strongly benefit from a multiparametric analysis. For instance, combining spectral and lifetime
641 detection schemes would provide additional contrast for photons detected in the same spectral
642 bin. This improvement could expand the range of detectable relative concentrations or might
643 allow further multiplexing of FFS.
644 Conventional two-color scanning FCCS has been previously applied to quantify receptor-ligand
645 interactions in living zebrafish embryos (12) and CRISPR/Cas9 edited cell lines to study such
646 interactions at endogenous protein level (45). SFSCS is thus directly applicable in the complex
647 environment of living multicellular organisms. In this context, spectral information could be
648 further exploited to separate low signal levels of endogenously expressed, fluorescently tagged
649 proteins from autofluorescence background.
650 As a first biological application of SFSCS, we investigated the interaction of IAV matrix protein
651 M2 with two cellular host factors: the tetraspanin CD9 and the autophagosome protein LC3.

652 We observed strong association of LC3 with M2, and consequent recruitment of LC3 to the PM
653 (Fig.S7), in agreement with previous *in vitro* and localization studies (34). Interestingly,
654 molecular brightness analysis reported oligomerization (dimers to tetramers) of M2, but
655 indicated a monomeric state of LC3 at the PM, i.e. binding of LC3 to M2 in an apparent
656 stoichiometry of 1:2 to 1:4. However, each M2 monomer provides a binding site for LC3 in the
657 cytoplasmic tail (46). A more detailed analysis of our data showed that in the analyzed cells
658 (i.e. cells showing clear membrane recruitment of LC3, Fig.S7A,B), the PM concentration of
659 LC3 was on average only 30% compared to that of M2 (Fig.S7C), although both proteins were
660 expressed in comparable amounts in the sample in general. This suggests that not all potential
661 binding sites in the cytoplasmic tail of M2 may be available to fluorescently tagged LC3, either
662 due to binding of endogenous LC3, other cellular host factors, or steric hindrance. In contrast
663 to the case of LC3, we did not detect significant binding of M2 with the tetraspanin CD9, a
664 protein that was previously shown to be incorporated into IAV virions and supposedly plays a
665 functional role during the infection process (47, 48). In future studies, the approach presented
666 here may be used to further elucidate the complex interaction network of viral proteins, e.g.
667 matrix protein 1 (M1) (49), M2, HA, and neuraminidase, cellular host factors, and PM lipids
668 (50) during the assembly process of IAV at the PM of living cells (51).
669 Finally, we demonstrated that RSICS allows the quantification of the stoichiometry of higher
670 order molecular complexes, based on molecular brightness analysis for each FP species. As
671 example of an application in a biological context, we determined the stoichiometry of the IAV
672 PC. Our data provide strong evidence for a 2:2:2 stoichiometry of the PC subunits PA, PB1 and
673 PB2, i.e. dimerization of hetero-trimeric PCs. Such interactions were previously proposed
674 based on experiments in solution using X-ray crystallography and cryo-electron microscopy
675 (52), co-immunoprecipitation assays (53, 54), as well as single channel brightness analysis of
676 FCCS data (for the PA subunit) (36). Intermolecular interactions in the PC are hypothesized to
677 be required for the initiation of vRNA synthesis during replication of the viral genome (52, 55).

678 The results presented here provide the first quantification of these interactions in living cells,
679 and a direct estimate of the stoichiometry of PCs in the cell nucleus. The formation of ternary
680 PC complexes in these samples could be extrapolated from the observed high rel.cc. values for
681 all three pair combinations, indicating very low amounts of unbound PA, PB1 or PB2 and
682 higher order interactions (see SI, paragraph 1 for additional details). Furthermore, this
683 observation could also be directly confirmed by performing, for the first time in living cells, a
684 triple correlation analysis (TRICS), indicating the presence of a considerable amount of PA-
685 PB1-PB2 complexes. It is worth noting though that the detection of coincident triple
686 fluctuations is prone to considerable noise and thus still limited to molecular complexes present
687 at low concentration and characterized by high molecular brightness for each fluorophore
688 species (21, 56).
689 Of note, the RSICS approach presented here provides for the first time simultaneous
690 information on molecular interactions, molecular brightness (and thus stoichiometry), diffusion
691 dynamics, and concentration for all three complex subunits. This specific feature opens the
692 possibility of a more in-depth analysis. For example, it is possible to quantify the relative cross-
693 correlation of two subunits, e.g. PA and PB2, as a function of the relative concentration of the
694 third subunit, e.g. PB1 (Fig.S9A). Similarly, molecular brightness and diffusion coefficients
695 can be analyzed as a function of the abundance of each subunit (Fig.S9B,C). With this approach,
696 it is therefore possible to distinguish specific molecular mechanism, e.g. inefficient PA-PB2
697 interactions in the presence of low PB1 concentration or efficient hetero-trimer dimerization
698 when all subunits are present at similar concentrations. The employed experimental scheme
699 offers a powerful tool for future studies, exploring, for example, interaction of the PC with
700 cellular host factors or the development of inhibitors that could interfere with the assembly
701 process of the complex, as a promising therapeutic target for antiviral drugs (57).
702 In conclusion, we present here three-species and, for the first time, four-species measurements
703 of protein interactions and diffusion dynamics in living cells. This is achieved by combining

704 and extending existing FFS techniques with spectrally resolved detection. The presented
705 approaches provide a powerful toolbox to investigate complex protein interaction networks in
706 living cells and organisms.
707
708
709

710 # MATERIALS AND METHODS

711 ## Cell culture and sample preparation

712 Human embryonic kidney (HEK) cells from the 293T line (purchased from ATCC®, Manassas,
713 VA, USA, CRL-3216TM) and human epithelial lung cells A549 (ATCC®, CCL-185TM) were
714 cultured in Dulbecco's modified Eagle medium (DMEM) with the addition of fetal bovine
715 serum (10%) and L-Glutamine (2 mM). Cells were passaged every 3–5 days, no more than 15
716 times. All solutions, buffers and media used for cell culture were purchased from PAN-Biotech
717 (Aidenbach, Germany).
718 For microscopy experiments, 3×10^5 (HEK) or 4×10^5 (A549) cells were seeded in 35 mm
719 #1.5 optical glass bottom dishes (CellVis, Mountain View, CA, USA) 24 h before transfection.
720 Cells were transfected 16–24 h prior to the experiment using between 50 ng and 150 ng plasmid
721 per dish with Turbofect (HEK) or Lipofectamin3000 (A549) according to the manufacturer's
722 instructions (Thermo Fisher Scientific, Waltham, MA, USA). Briefly, plasmids were incubated
723 for 20 min with 3 µl Turbofect diluted in 50 µl serum-free medium, or 15 min with 2 µl P3000
724 and 2 µl Lipofectamine3000 diluted in 100 µl serum-free medium, and then added dropwise to
725 the cells. For spectral imaging at different pH values, culture medium was exchanged with
726 buffer containing 140 mM NaCl, 2.5 mM KCl, 1.8 mM $CaCl_2$, 1.0 mM $MgCl_2$, and 20 mM
727 HEPES with pH ranging from 5.0 to 9.2.
728

729 ## Plasmids and cloning

730 The plasmids encoding FPs linked to a myristoylated and palmitoylated peptide (mp-mEGFP,
731 mp-mEYFP, mp-mCherry2, mp-2x-mEGFP), the full length IAV A/chicken/FPV/Rostock/
732 1934 hemagglutinin (HA) construct HA-mEGFP, and the plasmids for cytosolic expression of
733 mEGFP, mEYFP, mCherry2, 2x-mEGFP, 2x-mEYFP, 2x-mCherry2 and mCherry2-mEGFP
734 hetero-dimers were previously described (14) and are available on Addgene.

735 For the cloning of all following constructs, standard PCRs with custom-designed primers were
736 performed, followed by digestion with fast digest restriction enzymes and ligation with T4-
737 DNA-Ligase according to the manufacturer's instructions. All enzymes and reagents were
738 purchased from Thermo Fisher Scientific, Waltham, MA, USA.
739 To obtain mp-mEGFP-mEYFP, a mp-mEGFP_pcDNA3.1+ vector was first generated by
740 amplifying mp-mEGFP insert from the respective plasmid, and inserting it into pcDNA3.1+
741 vector (obtained from Thermo Fisher Scientific) by digestion with NheI and AflII. Afterwards,
742 mEYFP was amplified from mp-mEYFP, and inserted into mp-mEGFP_pcDNA3.1+ using
743 digestion with AflII and KpnI. To clone mp-mEYFP-(L)-mEGFP (a plasmid encoding for mp-
744 mEYFP-mEGFP hetero-dimers with a long rigid linker peptide (L) between FPs), a mp-
745 mEYFP-(L)_pcDNA3.1+ construct was first generated by amplifying mp-mEYFP from the
746 respective plasmid with primers encoding for the rigid linker (see Table S2 for linker peptide
747 sequences) and inserting it into pcDNA3.1+ vector by digestion with NheI and AflII. Then,
748 mEGFP was inserted from mEGFP-(L)_pcDNA3.1+ (see below) by digestion with KpnI and
749 BamHI. To generate mp-mEYFP-(L)-mCherry2-(L)-mEGFP, a mp-mEYFP-(L)-mCherry2-(L)
750 construct was first cloned by amplifying mCherry2 from a mCherry2-C1 vector (a gift from
751 Michael Davidson, Addgene plasmid # 54563) and inserting it into mp-mEYFP-
752 (L)_pcDNA3.1+ by digestion with AflII and KpnI. Subsequently, mEGFP was inserted from
753 mEGFP-(L)_pcDNA3.1+ (see below) using KpnI and BamHI restriction. The mp-mEYFP-(L)-
754 mCherry2-(L)-mEGFP-(L)-mApple plasmid was generated by inserting an mEGFP-(L)-
755 mApple cassette into mp-mEYFP-(L)-mCherry2-(L) by digestion with KpnI and EcoRI. The
756 mEGFP-(L)-mApple construct was cloned beforehand by amplifying mApple from PMT-
757 mApple (39) (a kind gift from Thorsten Wohland) and inserting it into mEGFP-
758 (L)_pcDNA3.1+ by digestion with BamHI and EcoRI. The mEGFP-(L)_pcDNA3.1+ plasmid
759 was obtained by amplifying mEGFP from an mEGFP-N1 vector (a gift from Michael Davidson,
760 Addgene plasmid # 54767) (using a primer encoding a long rigid linker sequence) and inserting

761 it into a pcDNA3.1+ vector by KpnI and BamHI restriction. The mApple_pcDNA3.1+ plasmid
762 was generated by amplifying mApple from PMT-mApple and inserting it into pcDNA3.1+
763 vector by digestion with KpnI and BamHI. The mp-mApple plasmid was generated by
764 amplifying mApple from PMT-mApple, and inserting it into mp-mCherry2 by digestion with
765 AgeI and BsrGI. To clone mp-mCherry2-(L)-mApple, a mp-mCherry2-(L)_pcDNA3.1+
766 plasmid was first generated by amplifying mp-mCherry2 (using a primer encoding a long rigid
767 linker sequence) and inserting it into pcDNA3.1+ using NheI and KpnI restriction. Afterwards,
768 mApple was amplified from PMT-mApple and inserted into mp-mCherry2-(L)_pcDNA3.1+
769 by digestion with KpnI and EcoRI. The mp-mCherry2-mEGFP plasmid was cloned by inserting
770 mp from mp-mEGFP into mCherry2-mEGFP, using digestion with NheI und AgeI. The
771 plasmids mEYFP-(L)-mApple, mEYFP-(L)-mCherry2-(L)-mEGFP and mEYFP-(L)-
772 mCherry2-(L)-mEGFP-(L)-mApple were generated by amplifying the respective insert from
773 mp-mEYFP-(L)-mApple, mp-mEYFP-(L)-mCherry2-(L)-mEGFP or mp-mEYFP-(L)-
774 mCherry2-(L)-mEGFP-(L)-mApple and inserting it into pcDNA3.1+ vector by digestion with
775 NheI and XbaI. The mp-mEYFP-(L)-mApple construct was cloned beforehand by inserting
776 mApple from mEGFP-(L)-mApple into mp-mEYFP-(L)_pcDNA3.1+ using restriction by
777 BamHI and EcoRI.

778 The CD9-mEGFP plasmid was cloned by amplifying CD9 from pCMV3-CD9 (obtained from
779 SinoBiological #HG11029-UT, encoding human CD9) and inserting into an mEGFP-C1 vector
780 using restriction by HindIII and BamHI. The LC3-mEYFP plasmid was generated by inserting
781 mEYFP from an mEYFP-C1 vector into pmRFP-LC3 (58) (a gift from Tamotsu Yoshimori,
782 Addgene plasmid # 21075, encoding rat LC3) using digestion with NheI and BglII. Plasmid
783 M2-mCherry2 (mCherry2 fused to the extracellular terminus of matrix protein 2 from influenza
784 A/chicken/FPV/Rostock/1934) was cloned by inserting mCherry2 from an mCherry2-C1
785 vector into mEYFP-FPV-M2 (a kind gift from Michael Veit) using restriction by AgeI and

786 BsrGI. Plasmids encoding IAV polymerase subunits PA-mEYFP, PB1-mEGFP and PB2-
787 mCherry2 (from influenza A/human/WSN/1933) were a kind gift from Andreas Herrmann.
788 The plasmids GPI-mEYFP and GPI-EGFP were a kind gift from Roland Schwarzer. GPI-
789 mEGFP was cloned by amplifying mEGFP from an mEGFP-N1 vector and inserting it into
790 GPI-EGFP, using digestion with AgeI and BsrGI. To generate GPI-mApple and GPI-
791 mCherry2, mApple and mCherry2 inserts were amplified from PMT-mApple and mCherry2-
792 C1, respectively, and inserted into GPI-mEYFP using restriction by AgeI and BsrGI.

793 All plasmids generated in this work will be made available on Addgene.

794

795 **Confocal microscopy system**

796 Scanning fluorescence spectral correlation spectroscopy (SFSCS) and raster spectral image
797 correlation spectroscopy (RSICS) were performed on a Zeiss LSM880 system (Carl Zeiss,
798 Oberkochen, Germany) using a 40x, 1.2NA water immersion objective. For two-species
799 measurements, samples were excited with a 488 nm Argon laser (mEGFP, mEYFP) or a 561
800 nm diode laser (mCherry2, mApple). For three- and four-species measurements, both laser lines
801 were used. To split excitation and emission light, 488 nm (for two-species measurements with
802 mEGFP and mEYFP) or 488/561 nm (for measurements including mCherry2 and mApple)
803 dichroic mirrors were used. Fluorescence was detected in spectral channels of 8.9 nm (15
804 channels between 491 nm and 624 nm for two-species measurements on mEGFP, mEYFP; 14
805 channels between 571 nm and 695 nm for two-species measurements on mCherry2, mApple;
806 23 channels between 491 nm and 695 nm for three- and four-species measurements) on a 32
807 channel GaAsP array detector operating in photon counting mode. All measurements were
808 performed at room temperature.

809

810

811 **Scanning fluorescence spectral correlation spectroscopy (SFSCS)**

812 *Data acquisition*: For SFSCS measurements, a line scan of 256x1 pixels (pixel size 80 nm) was
813 performed perpendicular to the PM with 403.20 µs scan time. Typically, 450,000-600,000 lines
814 were acquired (total scan time ca. 2.5 to 4 min). Laser powers were adjusted to keep
815 photobleaching below 50% at maximum for all species (average signal decays were ca. 10%
816 for mEGFP, 30% for mEYFP, 40% for mApple and 20% for mCherry2). Typical excitation
817 powers were ca. 5.6 µW (488 nm) and ca. 5.9 µW (561 nm). Spectral scanning data were
818 exported as TIFF files (one file per three spectral channels), imported and analyzed in
819 MATLAB (The MathWorks, Natick, MA, USA) using custom-written code.

820 *Data analysis*: SFSCS analysis followed the scanning FCS scheme described previously (11,
821 59), combined with spectral decomposition of the fluorescence signal by applying the
822 mathematical framework of FLCS and FSCS (22, 23). Briefly, all scan lines were aligned as
823 kymographs and divided in blocks of 1000 lines. In each block, lines were summed up column-
824 wise and across all spectral channels, and the lateral position with maximum fluorescence was
825 determined. This position defines the membrane position in each block and was used to align
826 all lines to a common origin. Then, all aligned line scans were averaged over time and fitted
827 with a Gaussian function. The pixels corresponding to the PM were defined as pixels within ±
828 2.5SD of the peak. In each line and spectral channel these pixels were integrated, providing
829 membrane fluorescence time series $F^k(t)$ in each spectral channel k (m channels in total). These
830 time series were then temporally binned with a binning factor of two and subsequently
831 transformed into the contributions $F_i(t)$ of each fluorophore species i (i.e. one fluorescence
832 time series for each species) by applying the spectral filtering algorithm presented by Benda et
833 al. (22):

834 $$F_i(t) = \sum_{k=1}^{m} f_i^k F^k(t).$$

835 Spectral filter functions f_i^k were calculated based on reference emission spectra p_i^k that were
836 determined for each individual species *i* from single species measurements performed on each
837 day, using the same acquisition settings:

838 $$f_i^k = \left(\left[\widehat{M}^T D \widehat{M}\right]^{-1} \widehat{M} D\right)_{ik}.$$

839 Here, $\widehat{M}$ is a matrix with elements $M_{ki} = p_i^k$ and *D* is a diagonal matrix, $D = diag[1/\langle F^k(t)\rangle]$.
840 In order to correct for depletion due to photobleaching, a two-component exponential function
841 was fitted to the fluorescence time series for each spectral species, $F_i(t)$, and a correction
842 formula was applied (59, 60). Finally, autocorrelation functions (ACFs) and pair-wise cross-
843 correlation functions (CCFs) of fluorescence time series of species *i* and *j* were calculated as
844 follows, using a multiple tau algorithm:

845 $$G_i(\tau) = \frac{\langle \delta F_i(t) \delta F_i(t+\tau)\rangle}{\langle F_i(t)\rangle^2},$$

846 $$G_{i,j}(\tau) = \frac{\langle \delta F_i(t) \delta F_j(t+\tau)\rangle}{\langle F_i(t)\rangle \langle F_j(t)\rangle},$$

847 where $\delta F_i(t) = F_i(t) - \langle F_i(t)\rangle$.
848 To avoid artefacts caused by long-term instabilities or single bright events, CFs were calculated
849 segment-wise (10-20 segments) and then averaged. Segments showing clear distortions
850 (typically less than 25% of all segments) were manually removed from the analysis (59).
851 A model for two-dimensional diffusion in the membrane and Gaussian focal volume geometry
852 (11) was fitted to all CFs:

853 $$G(\tau) = \frac{1}{N}\left(1 + \frac{\tau}{\tau_d}\right)^{-1/2}\left(1 + \frac{\tau}{\tau_d S^2}\right)^{-1/2}$$

854 Here, the particle number *N* and thus $G(\tau)$ were restricted to positive values. In the fitting
855 procedure, this constraint can generate low, but positive correlation amplitudes even in the
856 absence of correlation, i.e. for CFs fluctuating around zero, due to noise. This issue causes small
857 positive correlation amplitudes that were observed for some measurements lacking significant
858 correlation.

859 To calibrate the focal volume, point FCS measurements with Alexa Fluor® 488 (Thermo Fisher
860 Scientific, Waltham, MA, USA) dissolved in water at 20 nM were performed at the same laser
861 power. The structure parameter S was fixed to the average value determined in calibration
862 measurements (typically between 4 to 8).
863 From the amplitudes of ACFs and CCFs, relative cross-correlation (rel.cc.) values were
864 calculated for all cross-correlation combinations:

865 $$rel.cc._{i,j} = max\left\{\frac{G_{i,j}(0)}{G_i(0)}, \frac{G_{i,j}(0)}{G_j(0)}\right\},$$

866
867 where $G_{i,j}(0)$ is the amplitude of the CCF of species i and j, and $G_i(0)$ the amplitude of the ACF
868 of species i. The molecular brightness was calculated by dividing the mean count rate detected
869 for each species i by the particle number N_i determined from the fit: $B_i = \frac{\langle F_i(t)\rangle}{N_i}$. From this
870 value, an estimate of the oligomeric state ε_i was determined by normalizing B_i by the average
871 molecular brightness $B_{i,1}$ of the corresponding monomeric reference, and, subsequently, by the
872 fluorescence probability $p_{f,i}$ for species i: $\varepsilon_i = \frac{B_i/B_{i,1}}{p_{f,i}} - 1$, as previously derived (14). The p_f
873 was previously characterized for several FPs, e.g. ca. 60% for mCherry2 (14).
874 The signal-to-noise ratio (SNR) of the ACFs was calculated by dividing ACF values by their
875 variance and summing over all points of the ACF. The variance of each point of the ACF was
876 calculated in the multiple tau algorithm (61).
877 To ensure statistical robustness of the SFSCS analysis and sufficient SNR, the analysis was
878 restricted to cells expressing all fluorophore species in comparable amounts, i.e. relative
879 average signal intensities of less than 1:10 (mEGFP/mEYFP) or 1:5 (mApple/mCherry2, three-
880 and four-species measurements).
881
882
883

884 **Raster spectral image correlation spectroscopy (RSICS)**

885 *Data acquisition:* RSICS measurements were performed as previously described (62). Briefly,
886 200-400 frames of 256x256 pixels were acquired with 50 nm pixel size (i.e. a scan area of
887 12.83x12.83 μm^2 through the midplane of cells), 2.05 µs or 4.10 µs pixel dwell time, 1.23 ms
888 or 2.46 ms line, and 314.57 ms or 629.14 ms frame time (corresponding to ca. 2 min total
889 acquisition time per measurement). Samples were excited at ca. 5.6 µW (488 nm) and 4.6 µW
890 (561 nm) excitation powers, respectively. Laser powers were chosen to maximize the signal
891 emitted by each fluorophore species but keeping photobleaching below 50% at maximum for
892 all species (average signal decays were ca. 10% for mEGFP, 15% for mEYFP, 40% for mApple
893 and 25% for mCherry2). Typical counts per molecule were ca. 25 kHz for mEGFP (G), 15-20
894 kHz for mEYFP (Y), 20-30 kHz for mApple (A), and 5-10 kHz for mCherry2 (Ch2). To obtain
895 reference emission spectra for each individual fluorophore species, four image stacks of 25
896 frames were acquired at the same imaging settings on single species samples on each day.

897 *Data analysis:* RSICS analysis followed the implementation introduced recently (27), which is
898 based on applying the mathematical framework of FLCS and FSCS (22, 23) to RICS. Four-
899 dimensional image stacks $I(x, y, t, k)$ (time-lapse images acquired in k spectral channels) were
900 imported in MATLAB (The MathWorks, Natick, MA, USA) from CZI image files using the
901 Bioformats package (63) and further analyzed using custom-written code. First, average
902 reference emission spectra were calculated for each individual fluorophore species from single-
903 species measurements. Four-dimensional image stacks were then decomposed into three-
904 dimensional image stacks $I_i(x, y, t)$ for each species i using the spectral filtering algorithm
905 presented by Schrimpf et al. (27) (following the mathematical framework given in the SFSCS
906 section). Cross-correlation RICS analysis was performed in the arbitrary region RICS
907 framework (35). To this aim, a polygonal region of interest (ROI) was selected in the time- and
908 channel-averaged image frame containing a homogeneous region in the cytoplasm (four-
909 species measurements on FP constructs) or nucleus (three-species measurements on polymerase

complex and related controls) of cells. This approach allowed excluding visible intracellular organelles or pixels in the extracellular space, but to include all pixels containing signal from the nucleus of cells. In some cells, nucleus and cytoplasm could not be clearly distinguished. In these cases, all pixels were selected and minor brightness differences between cytoplasm and nucleus, previously found to be ca. 10% (14), were neglected. Image stacks were further processed with a high-pass filter (with a moving 4-frame window) to remove slow signal variations and spatial inhomogeneities. Afterwards, RICS spatial ACFs and pair-wise CCFs were calculated for each image stack and all combinations of species *i, j* (e.g. G and Y, G and Ch2, Y and Ch2 for three species), respectively (27, 35):

$$G_i(\xi,\psi) = \frac{\langle \delta I_i(x,y)\delta I_i(x+\xi,y+\psi)\rangle}{\langle I_i(x,y)\rangle^2},$$

$$G_{i,j}(\xi,\psi) = \frac{\langle \delta I_i(x,y)\delta I_j(x+\xi,y+\psi)\rangle}{\langle I_i(x,y)\rangle\langle I_j(x,y)\rangle},$$

where $\delta I_i(x,y) = I_i(x,y) - \langle I_i(x,y)\rangle$.

ACF amplitudes were corrected as described in (35) to account for the effect of the high-pass filter. A three-dimensional normal diffusion RICS fit model (5, 6) for Gaussian focal volume geometry (with particle number *N*, diffusion coefficient *D*, waist ω_0, structure parameter *S* as free fit parameters, and fixed shape factor $\gamma = 2^{-3/2}$ (27)) was then fitted to both, ACFs and CCFs:

$$G(\xi,\psi) = \frac{\gamma}{N}\left(1+\frac{4D|(\xi-\xi_0)\tau_p+\psi\tau_l|}{\omega_0^2}\right)^{-1}\left(1+\frac{4D|(\xi-\xi_0)\tau_p+\psi\tau_l|}{\omega_0^2 S^2}\right)^{-1/2} exp\left(-\frac{\delta s^2((\xi-\xi_0)^2+\psi^2)}{\omega_0^2+4D|(\xi-\xi_0)\tau_p+\psi\tau_l|}\right),$$

where τ_p, τ_l denote the pixel dwell and line time and δs the pixel size. The free parameter ξ_0 (starting value = 13 pixels) was used to determine which CCFs were too noisy (i.e. $\xi_0 > 4$ pixels) to obtain meaningful parameters (typically in the absence of interaction). For ACF analysis, ξ_0 was set to 0. To remove shot noise contributions, the correlation at zero lag time was omitted from the analysis.

From the fit amplitudes of the ACFs and CCFs, rel.cc. values were calculated:

934 $$rel.cc._{i,j} = max\left\{\frac{G_{i,j}(0,0)}{G_i(0,0)}, \frac{G_{i,j}(0,0)}{G_j(0,0)}\right\},$$

935 where $G_{i,j}(0,0)$ is the amplitude of the CCF of species i and j, and $G_i(0,0)$ the ACF amplitude
936 of species i. In the case of non-meaningful convergence of the fit to the CCFs (i.e. $\xi_0 > 4$
937 pixels), the rel.cc. was simply set to 0. To ensure statistical robustness of the RSICS analysis
938 and sufficient SNR, the analysis was restricted to cells expressing all fluorophore species in
939 comparable amounts, i.e. relative average signal intensities of less than 1:6 for all species (in
940 all RSICS experiments). The molecular brightness of species i was calculated by dividing the
941 average count rate in the ROI by the particle number determined from the fit to the ACF: $B_i =$
942 $\frac{\langle I_i(t)\rangle}{N_i}$. From this value, an estimate of the oligomeric state ε_i was determined by normalizing B_i
943 by the average molecular brightness $B_{i,1}$ of the corresponding monomeric reference, and,
944 subsequently, by the fluorescence probability $p_{f,i}$ for species i: $\varepsilon_i = \frac{B_i/B_{i,1}}{p_{f,i}} - 1$, as previously
945 derived (14). The p_f was calculated from the obtained molecular brightness $B_{i,2}$ of FP homo-
946 dimers of species i: $p_f = \frac{B_{i,1}}{B_{i,2}} - 1$ (14).

947

948 **Triple raster image correlation spectroscopy (TRICS) analysis**

949 TRICS was performed using three-dimensional RSICS image stacks $I_i(x, y, t)$ detected for
950 three species i. First, the spatial triple correlation function (3CF) was calculated:

951 $$G_{1,2,3}(\xi_1, \psi_1, \xi_2, \psi_2) = \frac{\langle \delta I_i(x,y)\delta I_j(x+\xi_1,y+\psi_1)\delta I_k(x+\xi_2,y+\psi_2)\rangle}{\langle I_i(x,y)\rangle\langle I_j(x,y)\rangle\langle I_k(x,y)\rangle},$$

952 where ξ_1, ξ_2 denote spatial lags along lines and ψ_1, ψ_2 along columns of the image stacks.
953 Contributions from δI triplets containing at least two intensity values from the same pixel
954 position were not included in the calculation, in order to avoid shot-noise artefacts (since all
955 channels are detected here by the same detector). From the resulting four-dimensional matrix,
956 a two-dimensional representation was calculated by introducing coordinates a, b for the
957 effective spatial shift between signal fluctuations evaluated for the two species combinations:

$$a = ceil\left(\sqrt{{\xi_1}^2 + {\xi_2}^2}\right),$$

$$b = ceil\left(\sqrt{{\psi_1}^2 + {\psi_2}^2}\right).$$

The four-dimensional triple correlation matrix was transformed into a two-dimensional representation $G_{3C}(a,b)$ by rounding up a and b to integer values and averaging all points with the same rounded spatial shift. For example, for a 1-pixel shift along a line in one FP channel and a 1-pixel shift along a column in the third FP channel (i.e. $\xi_1 = 1, \psi_1 = 0, \xi_2 = 0, \psi_2 = 1$), a=b=1. $G_{3C}(1,1)$ also includes in its averaged value the other seven correlation values corresponding e.g. to $(\xi_1 = 0, \psi_1 = 1, \xi_2 = 1, \psi_2 = 0)$, $(\xi_1 = 1, \psi_1 = 0, \xi_2 = 0, \psi_2 = -1)$ and so on. As a further example, $G_{3C}(2,0)$ includes and averages only the two correlation values corresponding to $\psi_1 = \psi_2 = 0$ (i.e. no shift along columns) and $\xi_1 = -\xi_2 = \pm 1$ (i.e. a 1-pixel shift along a line, in opposite directions for the two channels). Note that the combinations $(\psi_1 = \psi_2 = 0, \xi_1 = \pm 2, \xi_2 = 0)$ and $(\psi_1 = \psi_2 = 0, \xi_1 = 0, \xi_2 = \pm 2)$ would also result in a=2 and b=0, but these values were not included since they refer to a correlation between identical pixel positions (e.g. $\xi_2 = 0, \psi_2 = 0$) between two FP channels and would be influenced by shot-noise artefacts (see above).

To determine the triple correlation amplitude $G_{3C}(0,0)$, the closest points (e.g. $G_{3C}(1,1)$, $G_{3C}(1,2)$, $G_{3C}(2,1)$, $G_{3C}(2,2)$, $G_{3C}(3,0)$) of the two-dimensional triple correlation were averaged, as an (slightly underestimated) approximation of the amplitude value at (0,0). Note that we chose not to include $G_{3C}(2,0)$ because this point is the average of only two possible spatial shift combinations, resulting in large statistical noise. Also, the point $G_{3C}(0,3)$ was not included since it refers to shifts along columns (i.e. the slow scanning direction) which, in turn, are characterized by a steeper decrease in amplitude. Finally, for best visualization, G_{3C} is plotted for a and b values ≥1 (see Figs. 7 and S2).

To account for reduction of the triple correlation amplitude due to the high-pass filter, an empirical correction was applied based on simulated triple correlation amplitudes with different sizes ΔF of the moving window (see SI, paragraph 2 and Fig.S1). Notably, applying this empirical correction to the auto- and cross-correlation amplitudes confirmed the previously introduced correction formula (see Fig.S1), $G_{corr}(\xi,\psi) = \frac{\Delta F}{\Delta F - 1} G(\xi,\psi)$ (35). The triple correlation amplitude is related to the number of triple complexes N_{3C} (20, 64):

$$G_{3C}(0,0) = \frac{4N_{3C}}{3N_1N_2N_3} = \frac{4N_{3C}}{3} G_1(0,0)G_2(0,0)G_3(0,0),$$

where N_i is the total number of proteins detected for species i. In analogy to the rel.cc., a relative triple correlation rel.3C. is defined, quantifying the fraction of triple complexes relative to the total number of proteins of the species that is present in the lowest concentration:

$$rel.3C. = max\left\{\frac{N_{3C}}{N_1}, \frac{N_{3C}}{N_2}, \frac{N_{3C}}{N_3}\right\} = \frac{3}{4}\frac{G_{3C}(0,0)}{G_1(0,0)G_2(0,0)G_3(0,0)} max\{G_1(0,0), G_2(0,0), G_3(0,0)\}.$$

Statistical Analyses

All data are displayed as scatter dot plots indicating mean values and SDs. Sample size is given in parentheses in each graph. Statistical significance was tested using Welch's corrected two-tailed student's t-test in GraphPad Prism 7.0 (GraphPad Software) and p-values are given in figure captions.

AUTHOR CONTRIBUTIONS

Research planning, V.D. and S.C; investigation, V.D. and A.P; data analysis, V.D. and S.C.; writing-original draft preparation, V.D. and S.C.; writing-review and editing, A.P.; software, V.D. and S.C.; supervision, S.C.; funding acquisition, S.C.

1005 **ACKNOWLEDGEMENTS**

1006 This work was financed by the DFG 254850309 grant to S.C. The LSM 880 instrumentation
1007 was funded by the German Research Foundation (DFG) grant INST 336/114-1 FUGG. The
1008 authors kindly thank Madlen Luckner for providing the plasmids for PA-mEYFP, PB1-mEGFP
1009 and PB2-mCherry2 expression, Thorsten Wohland for providing the PMT-mApple plasmid and
1010 Jelle Hendrix for fruitful discussion.

1011

1012

1013 **REFERENCES**

1014 1. Jameson, D.M., J.A. Ross, and J.P. Albanesi. 2009. Fluorescence
1015 fluctuation spectroscopy: ushering in a new age of enlightenment for
1016 cellular dynamics. *Biophys. Rev.* 1:105–118.

1017 2. Weidemann, T., J. Mücksch, and P. Schwille. 2014. Fluorescence
1018 fluctuation microscopy: a diversified arsenal of methods to investigate
1019 molecular dynamics inside cells. *Curr. Opin. Struct. Biol.* 28:69–76.

1020 3. Petazzi, R.A., A.K. Aji, and S. Chiantia. 2020. Fluorescence microscopy
1021 methods for the study of protein oligomerization. In: Progress in
1022 Molecular Biology and Translational Science. Elsevier B.V. pp. 1–41.

1023 4. Schwille, P., F.J. Meyer-Almes, and R. Rigler. 1997. Dual-color
1024 fluorescence cross-correlation spectroscopy for multicomponent
1025 diffusional analysis in solution. *Biophys. J.* 72:1878–1886.

1026 5. Digman, M.A., C.M. Brown, P. Sengupta, P.W. Wiseman, A.R. Horwitz,
1027 and E. Gratton. 2005. Measuring fast dynamics in solutions and cells with

1028 a laser scanning microscope. *Biophys. J.* 89:1317–27.

1029 6. Digman, M.A., P.W. Wiseman, A.R. Horwitz, and E. Gratton. 2009.
1030 Detecting protein complexes in living cells from laser scanning confocal
1031 image sequences by the cross correlation raster image spectroscopy
1032 method. *Biophys. J.* 96:707–16.

1033 7. Digman, M. a, R. Dalal, A.F. Horwitz, and E. Gratton. 2008. Mapping the
1034 number of molecules and brightness in the laser scanning microscope.
1035 *Biophys. J.* 94:2320–2332.

1036 8. Digman, M.A., P.W. Wiseman, C. Choi, A.R. Horwitz, and E. Gratton.
1037 2009. Stoichiometry of molecular complexes at adhesions in living cells.
1038 *Proc. Natl. Acad. Sci. U. S. A.* 106:2170–2175.

1039 9. Krieger, J.W., A.P. Singh, N. Bag, C.S. Garbe, T.E. Saunders, J.
1040 Langowski, and T. Wohland. 2015. Imaging fluorescence (cross-)
1041 correlation spectroscopy in live cells and organisms. *Nat. Protoc.*
1042 10:1948–1974.

1043 10. Magde, D., E. Elson, and W.W. Webb. 1972. Thermodynamic
1044 Fluctuations in a Reacting System - Measurement by Fluorescence
1045 Correlation Spectroscopy. *Phys. Rev. Lett.* 29:705–708.

1046 11. Ries, J., and P. Schwille. 2006. Studying Slow Membrane Dynamics with
1047 Continuous Wave Scanning Fluorescence Correlation Spectroscopy.
1048 *Biophys. J.* 91:1915–1924.

1049 12. Ries, J., S.R. Yu, M. Burkhardt, M. Brand, and P. Schwille. 2009. Modular

1050 scanning FCS quantifies receptor-ligand interactions in living multicellular
1051 organisms. *Nat. Methods*. 6.
1052 13. Dunsing, V., M. Mayer, F. Liebsch, G. Multhaup, and S. Chiantia. 2017.
1053 Direct evidence of amyloid precursor-like protein 1 trans interactions in
1054 cell-cell adhesion platforms investigated via fluorescence fluctuation
1055 spectroscopy. *Mol. Biol. Cell*. 28:3609–3620.
1056 14. Dunsing, V., M. Luckner, B. Zühlke, R.A. Petazzi, A. Herrmann, and S.
1057 Chiantia. 2018. Optimal fluorescent protein tags for quantifying protein
1058 oligomerization in living cells. *Sci. Rep.* 8:10634.
1059 15. Galperin, E., V. V Verkhusha, and A. Sorkin. 2004. Three-chromophore
1060 FRET microscopy to analyze multiprotein interactions in living cells. *Nat.*
1061 *Methods*. 1:209–217.
1062 16. Sun, Y., H. Wallrabe, C.F. Booker, R.N. Day, and A. Periasamy. 2010.
1063 Three-Color Spectral FRET Microscopy Localizes Three Interacting
1064 Proteins in Living Cells. *Biophys. J.* 99:1274–1283.
1065 17. Hur, K.H., Y. Chen, and J.D. Mueller. 2016. Characterization of Ternary
1066 Protein Systems in Vivo with Tricolor Heterospecies Partition Analysis.
1067 *Biophys. J.* 110:1158–1167.
1068 18. Burkhardt, M., K.G. Heinze, and P. Schwille. 2005. Four-color
1069 fluorescence correlation spectroscopy realized in a grating-based detection
1070 platform. *Opt. Lett.* 30:2266.
1071 19. Hwang, L.C., M. Gösch, T. Lasser, and T. Wohland. 2006. Simultaneous

1072 Multicolor Fluorescence Cross-Correlation Spectroscopy to Detect Higher
1073 Order Molecular Interactions Using Single Wavelength Laser Excitation.
1074 *Biophys. J.* 91:715–727.
1075 20. Heinze, K.G., M. Jahnz, and P. Schwille. 2004. Triple-Color Coincidence
1076 Analysis: One Step Further in Following Higher Order Molecular
1077 Complex Formation. *Biophys. J.* 86:506–516.
1078 21. Ridgeway, W.K., D.P. Millar, and J.R. Williamson. 2012. Quantitation of
1079 ten 30S ribosomal assembly intermediates using fluorescence triple
1080 correlation spectroscopy. *Proc. Natl. Acad. Sci. U. S. A.* 109:13614–
1081 13619.
1082 22. Benda, A., P. Kapusta, M. Hof, and K. Gaus. 2014. Fluorescence spectral
1083 correlation spectroscopy (FSCS) for probes with highly overlapping
1084 emission spectra. *Opt. Express*. 22:2973.
1085 23. Böhmer, M., M. Wahl, H.J. Rahn, R. Erdmann, and J. Enderlein. 2002.
1086 Time-resolved fluorescence correlation spectroscopy. *Chem. Phys. Lett.*
1087 353:439–445.
1088 24. Kapusta, P., M. Wahl, A. Benda, M. Hof, and J. Enderlein. 2007.
1089 Fluorescence lifetime correlation spectroscopy. *J. Fluoresc.* 17:43–48.
1090 25. Ghosh, A., N. Karedla, J.C. Thiele, I. Gregor, and J. Enderlein. 2018.
1091 Fluorescence lifetime correlation spectroscopy: Basics and applications.
1092 *Methods*. 140–141:32–39.
1093 26. Padilla-Parra, S., N. Audugé, M. Coppey-Moisan, and M. Tramier. 2011.

1094 Dual-color fluorescence lifetime correlation spectroscopy to quantify
1095 protein-protein interactions in live cell. *Microsc. Res. Tech.* 74:788–793.
1096 27. Schrimpf, W., V. Lemmens, N. Smisdom, M. Ameloot, D.C. Lamb, and J.
1097 Hendrix. 2018. Crosstalk-free multicolor RICS using spectral weighting.
1098 *Methods*. 140–141:97–111.
1099 28. Štefl, M., K. Herbst, M. Rübsam, A. Benda, and M. Knop. 2020. Single-
1100 Color Fluorescence Lifetime Cross-Correlation Spectroscopy In Vivo.
1101 *Biophys. J.* 119:1359–1370.
1102 29. Foo, Y.H., N. Naredi-Rainer, D.C. Lamb, S. Ahmed, and T. Wohland.
1103 2012. Factors affecting the quantification of biomolecular interactions by
1104 fluorescence cross-correlation spectroscopy. *Biophys. J.* 102:1174–83.
1105 30. Foust, D.J., A.G. Godin, A. Ustione, P.W. Wiseman, and D.W. Piston.
1106 2019. Two-Color Spatial Cumulant Analysis Detects Heteromeric
1107 Interactions between Membrane Proteins. *Biophys. J.* 117:1764–1777.
1108 31. Florin, L., and T. Lang. 2018. Tetraspanin assemblies in virus infection.
1109 *Front. Immunol.* 9:1140.
1110 32. Hantak, M.P., E. Qing, J.T. Earnest, and T. Gallagher. 2018. Tetraspanins:
1111 Architects of Viral Entry and Exit Platforms. *J. Virol.* 93.
1112 33. Dahmane, S., C. Doucet, A. Le Gall, C. Chamontin, P. Dosset, F. Murcy,
1113 L. Fernandez, D. Salas, E. Rubinstein, M. Mougel, M. Nollmann, and P.E.
1114 Milhiet. 2019. Nanoscale organization of tetraspanins during HIV-1
1115 budding by correlative dSTORM/AFM. *Nanoscale*. 11:6036–6044.

1116 34. Beale, R., H. Wise, A. Stuart, B.J. Ravenhill, P. Digard, and F. Randow.
1117 2014. A LC3-interacting motif in the influenza A virus M2 protein is
1118 required to subvert autophagy and maintain virion stability. *Cell Host*
1119 *Microbe*. 15:239–247.
1120 35. Hendrix, J., T. Dekens, W. Schrimpf, and D.C. Lamb. 2016. Arbitrary-
1121 Region Raster Image Correlation Spectroscopy. *Biophys. J.* 111:1785–
1122 1796.
1123 36. Huet, S., S. V Avilov, L. Ferbitz, N. Daigle, S. Cusack, and J. Ellenberg.
1124 2010. Nuclear import and assembly of influenza A virus RNA polymerase
1125 studied in live cells by fluorescence cross-correlation spectroscopy. *J.*
1126 *Virol.* 84:1254–64.
1127 37. Kaliszewski, M.J., X. Shi, Y. Hou, R. Lingerak, S. Kim, P. Mallory, and
1128 A.W. Smith. 2018. Quantifying membrane protein oligomerization with
1129 fluorescence cross-correlation spectroscopy. *Methods*. 140–141:40–51.
1130 38. Shi, X., H.F. Yong, T. Sudhaharan, S.W. Chong, V. Korzh, S. Ahmed, and
1131 T. Wohland. 2009. Determination of dissociation constants in living
1132 zebrafish embryos with single wavelength fluorescence cross-correlation
1133 spectroscopy. *Biophys. J.* 97:678–686.
1134 39. Sankaran, J., H. Balasubramanian, W.H. Tang, X.W. Ng, A. Röllin, and T.
1135 Wohland. 2020. SRRF 'n' TIRF - FCS: Simultaneous spatiotemporal
1136 super-resolution microscopy. *bioRxiv*. 2020.02.26.965905.
1137 40. Cranfill, P.J., B.R. Sell, M.A. Baird, J.R. Allen, Z. Lavagnino, H.M. de

1138 Gruiter, G.-J. Kremers, M.W. Davidson, A. Ustione, and D.W. Piston.
1139 2016. Quantitative assessment of fluorescent proteins. *Nat. Methods*.
1140 13:557–562.
1141 41. Hendrix, J., C. Flors, P. Dedecker, J. Hofkens, and Y. Engelborghs. 2008.
1142 Dark states in monomeric red fluorescent proteins studied by fluorescence
1143 correlation and single molecule spectroscopy. *Biophys. J.* 94:4103–13.
1144 42. Bacia, K., Z. Petrášek, and P. Schwille. 2012. Correcting for spectral
1145 cross-talk in dual-color fluorescence cross-correlation spectroscopy.
1146 *ChemPhysChem*. 13:1221–1231.
1147 43. Müller, B.K., E. Zaychikov, C. Bräuchle, and D.C. Lamb. 2005. Pulsed
1148 Interleaved Excitation. *Biophys. J.* 89:3508–3522.
1149 44. Hendrix, J., W. Schrimpf, M. Höller, and D.C. Lamb. 2013. Pulsed
1150 Interleaved Excitation Fluctuation Imaging. *Biophys. J.* 105:848–861.
1151 45. Eckert, A.F., P. Gao, J. Wesslowski, X. Wang, J. Rath, K. Nienhaus, G.
1152 Davidson, and G.U. Nienhaus. 2020. Measuring ligand-cell surface
1153 receptor affinities with axial line-scanning fluorescence correlation
1154 spectroscopy. *Elife*. 9:1–92.
1155 46. Claridge, J.K., F. Mohd-Kipli, A. Florea, T. Gate, and J.R. Schnell. 2020.
1156 pH-dependent secondary structure propensity of the influenza A virus M2
1157 cytoplasmic tail. *Biomol. NMR Assign.* 14:157–161.
1158 47. Shaw, M.L., K.L. Stone, C.M. Colangelo, E.E. Gulcicek, and P. Palese.
1159 2008. Cellular Proteins in Influenza Virus Particles. *PLoS Pathog.*

1160 4:e1000085.
1161 48. Hutchinson, E.C., P.D. Charles, S.S. Hester, B. Thomas, D. Trudgian, M.
1162 Martínez-Alonso, and E. Fodor. 2014. Conserved and host-specific
1163 features of influenza virion architecture. *Nat. Commun.* 5:1–11.
1164 49. Hilsch, M., B. Goldenbogen, C. Sieben, C.T. Höfer, J.P. Rabe, E. Klipp,
1165 A. Herrmann, and S. Chiantia. 2014. Influenza A Matrix Protein M1
1166 Multimerizes upon Binding to Lipid Membranes. *Biophys. J.* 107:912–
1167 923.
1168 50. Bobone, S., M. Hilsch, J. Storm, V. Dunsing, A. Herrmann, and S.
1169 Chiantia. 2017. Phosphatidylserine lateral organization influences the
1170 interaction of influenza virus matrix protein 1 with lipid membranes. *J.*
1171 *Virol.* 91.
1172 51. Rossman, J.S., and R.A. Lamb. 2011. Influenza virus assembly and
1173 budding. *Virology*. 411:229–236.
1174 52. Fan, H., A.P. Walker, L. Carrique, J.R. Keown, I. Serna Martin, D. Karia,
1175 J. Sharps, N. Hengrung, E. Pardon, J. Steyaert, J.M. Grimes, and E. Fodor.
1176 2019. Structures of influenza A virus RNA polymerase offer insight into
1177 viral genome replication. *Nature*. 573:287–290.
1178 53. Jorba, N., E. Area, and J. Ortín. 2008. Oligomerization of the influenza
1179 virus polymerase complex in vivo. *J. Gen. Virol.* 89:520–524.
1180 54. Nilsson-Payant, B.E., J. Sharps, N. Hengrung, and E. Fodor. 2018. The
1181 Surface-Exposed PA 51-72 -Loop of the Influenza A Virus Polymerase Is

1182 Required for Viral Genome Replication . *J. Virol.* 92.
1183 55. Chen, K.-Y., E. Dos Santos Afonso, V. Enouf, C. Isel, and N. Naffakh.
1184 2019. Influenza virus polymerase subunits co-evolve to ensure proper
1185 levels of dimerization of the heterotrimer. *PLOS Pathog.* 15:e1008034.
1186 56. Ridgeway, W.K., D.P. Millar, and J.R. Williamson. 2012. The
1187 Spectroscopic Basis of Fluorescence Triple Correlation Spectroscopy. *J.*
1188 *Phys. Chem. B*. 116:1908–1919.
1189 57. Massari, S., J. Desantis, M.G. Nizi, V. Cecchetti, and O. Tabarrini. 2020.
1190 Inhibition of Influenza Virus Polymerase by Interfering with Its Protein–
1191 Protein Interactions. *ACS Infect. Dis.* acsinfecdis.0c00552.
1192 58. Kimura, S., T. Noda, and T. Yoshimori. 2007. Dissection of the
1193 autophagosome maturation process by a novel reporter protein, tandem
1194 fluorescent-tagged LC3. *Autophagy*. 3:452–460.
1195 59. Dunsing, V., and S. Chiantia. 2018. A Fluorescence Fluctuation
1196 Spectroscopy Assay of Protein-Protein Interactions at Cell-Cell Contacts.
1197 *J. Vis. Exp.* e58582.
1198 60. Ries, J., S. Chiantia, and P. Schwille. 2009. Accurate Determination of
1199 Membrane Dynamics with Line-Scan FCS. *Biophys. J.* 96:1999–2008.
1200 61. Wohland, T., R. Rigler, and H. Vogel. 2001. The standard deviation in
1201 fluorescence correlation spectroscopy. *Biophys. J.* 80:2987–99.
1202 62. Ziegler, M., K. Yserentant, V. Middel, V. Dunsing, A. Gralak, K. Pakari,
1203 J. Bargstedt, C. Kern, S. Chiantia, U. Strähle, D.-P. Herten, and R.

1204 Wombacher. 2020. A chemical strategy to control protein networks in
1205 vivo. *bioRxiv*. 2020.04.08.031427.
1206 63. Linkert, M., C.T. Rueden, C. Allan, J.-M. Burel, W. Moore, A. Patterson,
1207 B. Loranger, J. Moore, C. Neves, D. MacDonald, A. Tarkowska, C. Sticco,
1208 E. Hill, M. Rossner, K.W. Eliceiri, and J.R. Swedlow. 2010. Metadata
1209 matters: access to image data in the real world. *J. Cell Biol.* 189:777–782.
1210 64. Palmer, A.G., and N.L. Thompson. 1987. Molecular aggregation
1211 characterized by high order autocorrelation in fluorescence correlation
1212 spectroscopy. *Biophys. J.* 52:257–270.
1213
1214